bioRxiv preprint doi: https://doi.org/10.1101/2021.02.24.432816; this version posted February 25, 2021. The copyright holder for this preprint (which was not certified by peer review) is the author/funder, who has granted bioRxiv a license to display the preprint in perpetuity. It is made available under aCC-BY 4.0 International license.

Dual mechanisms of opioid-induced respiratory depression in the inspiratory rhythm-generating network

Nathan A Baertsch[1,2,*], Nicholas E Bush[1], Nicholas J Burgraff[1], and Jan-Marino Ramirez[1,2,3]

[1]Center for Integrative Brain Research; Seattle Children's Research Institute; Seattle, WA, USA

[2]Department of Pediatrics; University of Washington; Seattle, WA, USA

[3]Department Neurological Surgery; University of Washington; Seattle, WA, USA

*** Corresponding Author and Lead Contact:**

Nathan Baertsch

nathan.baertsch@seattlechildrens.org

(218)349-6757

Postal Address for all authors:

1900 9th Ave.

JMB10

Seattle, WA 98101

Author Contributions: Conceptualization, NAB; Methodology, NAB, NEB; Investigation, NAB, NEB, NJB; Formal Analysis, NAB, NJB; Writing–Original Draft, NAB; Writing–Review & Editing, NAB, NEB, NJB, JMR; Funding Acquisition, NAB, JMR; Visualization, NAB, NEB; Supervision, NAB, JMR.

Declarations of Interest: The authors declare no conflicts of interest.

bioRxiv preprint doi: https://doi.org/10.1101/2021.02.24.432816; this version posted February 25, 2021. The copyright holder for this preprint (which was not certified by peer review) is the author/funder, who has granted bioRxiv a license to display the preprint in perpetuity. It is made available under aCC-BY 4.0 International license.

Abstract

The analgesic utility of opioid-based drugs is limited by the life-threatening risk of respiratory depression. Opioid-induced respiratory depression (OIRD), mediated by the μ-opioid receptor (MOR), is characterized by a pronounced decrease in the frequency and regularity of the inspiratory rhythm, which originates from the medullary preBötzinger Complex (preBötC). To unravel the cellular- and network-level consequences of MOR activation in the preBötC, MOR-expressing neurons were optogenetically identified and manipulated in transgenic mice *in vitro* and *in vivo*. Based on these results, a model of OIRD was developed *in silico*. We conclude that hyperpolarization of MOR-expressing preBötC neurons alone does not phenocopy OIRD. Instead, the effects of MOR activation are twofold: 1) pre-inspiratory spiking is reduced and 2) excitatory synaptic transmission is suppressed, thereby disrupting network-driven rhythmogenesis. These dual mechanisms of opioid action act together to make the normally robust inspiratory-rhythm-generating network particularly prone to collapse when challenged with exogenous opioids.

bioRxiv preprint doi: https://doi.org/10.1101/2021.02.24.432816; this version posted February 25, 2021. The copyright holder for this preprint (which was not certified by peer review) is the author/funder, who has granted bioRxiv a license to display the preprint in perpetuity. It is made available under aCC-BY 4.0 International license.

Introduction

The neuronal control of breathing is highly vulnerable to exogenous opioid-based analgesics and drugs of abuse. As a result, clinical and illicit use of opioids is associated with the life-threatening, and often difficult to predict, risk for opioid-induced respiratory depression (OIRD) (Overdyk et al., 2014, Gupta et al., 2018, Dahan et al., 2018). Yet, opioids are widely used due to their powerful analgesic utility and their hedonic and addictive properties. In response to overdoses, naloxone (Narcan) remains the gold standard for reversal of OIRD. But, naloxone has limitations including a short half-life, loss of analgesia, rapid induction of withdrawal symptoms, and reduced efficacy against opioids with high affinity for the MOR, such as carfentanil and buprenorphine (Gal, 1989, Algera et al., 2019, Dahan et al., 2010, van Dorp et al., 2006).

This highlights the need to expand the toolbox of strategies to protect against and reverse OIRD while preserving the intended analgesic effects of opioids. Yet, to date, such strategies are limited. One approach has focused on the development of biased MOR agonists that limit activation of β-arrestin2-dependent signaling (Conibear and Kelly, 2019, Schmid et al., 2017). However, a role of β-arrestin2 in mediating the respiratory side effects of opioids has not been reproducible among laboratories (Kliewer et al., 2020, Kliewer et al., 2019), casting doubt on the potential for biased agonists to mitigate OIRD. A second approach involves the use of respiratory stimulants in combination with opioid medication as a compensatory strategy to protect against OIRD (Algera et al., 2019, Manzke et al., 2003, Imam et al., 2020). Such strategies have shown promise in animal models (Mosca et al., 2014, Kimura et al., 2015, Guenther et al., 2010, Ren et al., 2009, Sun et al., 2019, Haw et al., 2016, Dai et al., 2017) and in some human trials (Oertel et al., 2010, Persson et al., 1999) but not others (Lötsch et al., 2005, Oertel et al., 2007). Optimization of this approach will require a detailed mechanistic understanding of the physiological consequences of MOR activation in the respiratory network.

bioRxiv preprint doi: https://doi.org/10.1101/2021.02.24.432816; this version posted February 25, 2021. The copyright holder for this preprint (which was not certified by peer review) is the author/funder, who has granted bioRxiv a license to display the preprint in perpetuity. It is made available under aCC-BY 4.0 International license.

Thus, unravelling how opioids affect the respiratory control network represents a critical step towards combating the mortality associated with the opioid health crisis.

In humans and mice, OIRD is characterized by a pronounced decrease in the frequency and regularity of breaths (Bouillon et al., 2003, Ferguson and Drummond, 2006, Smart et al., 2000). This is primarily due to longer and more irregular pauses between inspiratory efforts (Drummond, 1983). Both the beneficial analgesic effects and the detrimental respiratory consequences of opioids are dependent on the $G\alpha_{i/o}$-coupled, μ-opioid receptor (MOR) encoded by the *Oprm1* gene (Dahan et al., 2001, Sora et al., 1997). *Oprm1* is expressed widely throughout the brain (Erbs et al., 2015) (Allen Brain Atlas), and multiple sites in the central and peripheral nervous system are important for modulating the severity of OIRD (Montandon et al., 2011, Kirby and McQueen, 1986, Prkic et al., 2012, Mustapic et al., 2010). Two brainstem sites important for respiratory control – the parabrachial nucleus (PBN) and the preBötzinger complex (preBötC) (Varga et al., 2020, Bachmutsky et al., 2020) are particularly important for understanding OIRD, since localized genetic deletions of *Oprm1* in these sites abolishes OIRD. The preBötC and PBN are bidirectionally connected (Yang and Feldman, 2018, Yang et al., 2020) yet have distinct functional roles in the control of breathing (Baertsch et al., 2018, Baertsch and Ramirez, 2019, Ramirez and Baertsch, 2018b). The preBötzinger Complex is an autonomously rhythmogenic hub for respiratory control, critical for producing the inspiratory rhythm per se (Del Negro et al., 2018, Smith et al., 1991a, Baertsch et al., 2018, Baertsch and Ramirez, 2019, Ramirez and Baertsch, 2018b, Ramirez et al., 1998, Tan et al., 2008), whereas the PBN is a powerful source of modulatory control, important for providing excitatory drive to the respiratory network and regulating respiratory phase relationships (Molkov et al., 2013, Levitt et al., 2015, Zuperku et al., 2017, Smith et al., 2013). Consequently, their respective roles in OIRD may be similarly distinct.

bioRxiv preprint doi: https://doi.org/10.1101/2021.02.24.432816; this version posted February 25, 2021. The copyright holder for this preprint (which was not certified by peer review) is the author/funder, who has granted bioRxiv a license to display the preprint in perpetuity. It is made available under aCC-BY 4.0 International license.

Here, we dissect the network- and cellular- level mechanisms of OIRD within the preBötC. The preBötC contains both excitatory and inhibitory neurons that interact to regulate breathing frequency (Winter et al., 2009, Baertsch et al., 2018). However, inhibitory synaptic transmission does not seem to play a significant role in OIRD (Bachmutsky et al., 2020, Gray et al., 1999a). Instead, excitatory glutamatergic neurons are the critical substrate for both rhythmogenesis and OIRD in the preBötC (Funk et al., 1993, Greer et al., 1991, Bachmutsky et al., 2020, Sun et al., 2019). Collectively, glutamatergic neurons produce an inspiratory rhythm with three distinct time-domains. Each respiratory cycle begins in a refractory phase, during which excitability within the preBötC network is reduced and the rhythm is relatively insensitive to perturbations (Baertsch et al., 2018, Kottick and Del Negro, 2015). The network then transitions to a percolation phase during which excitability gradually builds, driven by intrinsic membrane properties and synaptic excitation among recurrently connected neurons (Baertsch and Ramirez, 2019, Kam et al., 2013b). The percolation phase ends when network excitability becomes sufficiently high for interconnected preBötC neurons to produce a synchronized bout of action potentials during the third phase - a network-wide inspiratory burst. Together, the refractory and percolation phases define the time between inspiratory efforts, or inter-burst interval (IBI), which is the primary determinant of breathing frequency and regularity. Within the preBötC network, each neuron's firing pattern during the respiratory cycle, or "discharge identity" is largely determined by its synaptic inputs and intrinsic excitability. As a result, excitatory preBötC neurons are not functionally homogeneous (Ramirez and Baertsch, 2018a). Indeed, only a subset of preBötC neurons participate in all three phases of the inspiratory rhythm and are therefore considered particularly important mediators of rhythmogenesis (Kam et al., 2013a, Kam et al., 2013b, Baertsch and Ramirez, 2019, Rubin et al., 2009). These neurons, referred to as "pre-inspiratory neurons", are active during inspiratory bursts, suppressed during the refractory phase, and produce spikes during the percolation phase with a characteristic ramp in spike frequency (Baertsch and Ramirez, 2019, Baertsch et al., 2019). To

bioRxiv preprint doi: https://doi.org/10.1101/2021.02.24.432816; this version posted February 25, 2021. The copyright holder for this preprint (which was not certified by peer review) is the author/funder, who has granted bioRxiv a license to display the preprint in perpetuity. It is made available under aCC-BY 4.0 International license.

126 date, the effects of opioids on preBötC spiking activity and the three-phase inspiratory rhythm
127 have not been well defined, nor have the discharge identities of MOR-expressing preBötC
128 neurons.

129 To characterize mechanisms underlying OIRD in the preBötC, we combine *in vitro* and *in*
130 *vivo* electrophysiology and computational modelling approaches. Using optogenetic
131 identification and manipulation of *Oprm1* expressing neurons, we find that *Oprm1* is expressed
132 in ~50% of functionally identified preBötC neurons. In the context of OIRD, the activity of
133 *Oprm1*+ pre-inspiratory neurons is preferentially suppressed during the percolation phase.
134 However, mimicking this decrease in preBötC spiking is not sufficient to phenocopy OIRD.
135 Indeed, we find that, in addition to suppression of the number of spikes produced during the
136 percolation phase, excitatory pre-synaptic transmission from *Oprm1*+ neurons is also impaired
137 making the remaining spiking activity of these neurons less consequential for network function.
138 Based on these findings, we developed a computational model of the preBötC containing a
139 subpopulation of *Oprm1*+ neurons to isolate and compare the functional consequences of
140 membrane hyperpolarization with reduced pre-synaptic efficacy. Consistent with our
141 electrophysiology results, we find that OIRD is best modelled *in silico* when both mechanisms
142 occur in combination. We conclude that these dual mechanisms of opioid action in the preBötC
143 act together to make the inspiratory rhythm particularly vulnerable to exogenous opioids.

144

145 ## Results

146 ### *Phenotypes of Oprm1+ preBötC neurons*

147 Neurons in the inspiratory rhythm-generating network are functionally heterogeneous; and the
148 role of any given neuron is determined, in part, by its spiking pattern or “discharge identity”
149 (Segers et al., 2012). The inspiratory network is primarily composed of neurons with four

bioRxiv preprint doi: https://doi.org/10.1101/2021.02.24.432816; this version posted February 25, 2021. The copyright holder for this preprint (which was not certified by peer review) is the author/funder, who has granted bioRxiv a license to display the preprint in perpetuity. It is made available under aCC-BY 4.0 International license.

discharge identities that sum to produce the rhythmic activity observed in integrated multi-unit preBötC recordings: 1) *Pre-inspiratory neurons* with spiking during the inter-burst interval that ramps up prior to a bout of action potentials during inspiratory bursts. 2) *Inspiratory neurons* active only during inspiratory bursts. 3) A relatively small number of *"expiratory" neurons* (<15%, (Baertsch et al., 2019, Harris et al., 2017)) that receive more inhibitory input than excitatory input during bursts and only spike during the inter-burst interval; and 4) *tonic neurons* with spiking that is not modulated by the inspiratory rhythm. To identify the direct targets of MOR activation in the preBötC, we characterized the discharge identities of *Oprm1* expressing neurons within the preBötC using an *Oprm1*^{CreGFP} mouse line (heretofore referred to as *Oprm1*^{Cre}). Horizontal brainstem slices were prepared from *Oprm1*^{Cre}; *Rosa26*^{ChR2} and *Oprm1*^{Cre}; *Rosa26*^{ArchT} neonatal mice. Rhythmic integrated multi-unit activity was recorded simultaneously with single-unit activity (n=223) from the contralateral preBötC. The spiking pattern of each unit was referenced to the integrated multi-unit rhythm to determine its discharge identity, and the unit was subsequently characterized optogenetically as *Oprm1*+ or *Oprm1*- based on responses to light (Széll et al., 2020, Baertsch et al., 2018) (Figure 1A). The *Oprm1* gene was expressed in 52% of pre-inspiratory neurons, 42% of inspiratory neurons, 47% of expiratory neurons, and 60% of tonic neurons (Figure 1B, C). This leads to the first important conclusion that *Oprm1* is not preferentially expressed among neurons with a particular discharge identity. Of 58 neurons intracellularly labelled with AlexaFluor598 there was no spatial segregation of discharge identities or *Oprm1* expression in the preBötC (Figure 1D, E). These results are consistent with previous experiments that utilized *in situ* hybridization for *Oprm1* transcripts (Allen Brain Atlas; Supplemental Figure 1) and imaging of fluorescently tagged MOR (Erbs et al., 2015) suggesting that MOR-expressing neurons are numerous and broadly distributed in the preBötC region.

MOR activation reduces spiking during the percolation phase of the inspiratory rhythm.

bioRxiv preprint doi: https://doi.org/10.1101/2021.02.24.432816; this version posted February 25, 2021. The copyright holder for this preprint (which was not certified by peer review) is the author/funder, who has granted bioRxiv a license to display the preprint in perpetuity. It is made available under aCC-BY 4.0 International license.

Pre-inspiratory neurons are primarily excitatory (Baertsch et al., 2019) and play a critical role in rhythmogenesis (Del Negro et al., 2018, Del Negro et al., 2011, Ashhad and Feldman, 2020), frequency control, and regularity by participating in the percolation phase of the inspiratory rhythm (Baertsch and Ramirez, 2019). A prevailing view suggests that excitatory synaptic interactions among pre-inspiratory neurons within the recurrently connected preBötC network play a critical role in the percolation phase and together with intrinsic membrane properties and synaptic inhibition determine the resulting spiking activity. (Kam et al., 2013b, Del Negro and Hayes, 2008, Del Negro et al., 2011, Baertsch and Ramirez, 2019). To differentiate between the effects of MOR activation on the intrinsically- versus synaptically driven spiking activity in this important subgroup of preBötC neurons, we examined changes in the spiking of *Oprm1*+ and *Oprm1*- pre-inspiratory neurons while increasing the concentration of the MOR agonist DAMGO ([D-Ala2, N-MePhe4, Gly-ol]- enkephalin) before blocking excitatory synaptic transmission (AMPA- and NMDA-dependent) and reversing MOR activation with Naloxone (5 µM). The blockade of excitatory synaptic inputs revealed that most pre-inspiratory neurons (n=15/20, 75%) continued to spike tonically i.e., were “intrinsically tonic”, while others (n=5/20, 25%) became silent i.e., “intrinsically quiescent”, after blocking excitatory synaptic transmission. To estimate the contribution of intrinsic activity to pre-inspiratory spiking, we normalized the spike frequency during the inter-burst interval to the intrinsic spiking activity after blocking synaptic transmission: intrinsically driven (normalized spike frequency <~1) versus synaptically driven (normalized spike frequency >~1) for each individual neuron.

The intrinsic activity of each neuron was predictive of its response to DAMGO. DAMGO reduced (-60±13% at 300 nM), but did not eliminate, spiking during the inter-burst interval in *Oprm1*+ intrinsically tonic, pre-inspiratory neurons (Figure 2A, C, D). In contrast, the pre-inspiratory spiking of intrinsically tonic neurons that did not express MOR (*Oprm1*-) was much less affected by DAMGO (-11±10% at 300nM) (Figure 2A, C, D). Among intrinsically quiescent

bioRxiv preprint doi: https://doi.org/10.1101/2021.02.24.432816; this version posted February 25, 2021. The copyright holder for this preprint (which was not certified by peer review) is the author/funder, who has granted bioRxiv a license to display the preprint in perpetuity. It is made available under aCC-BY 4.0 International license.

neurons, pre-inspiratory spiking was significantly suppressed by DAMGO in both *Oprm1*+ and *Oprm1*- neurons (-95±5% and -57±9%, respectively) (Figure 2B, E, F). Collectively, these results suggest that MOR activation suppresses pre-inspiratory percolation activity within the preBötC.

Effects of MOR activation on preBötC neurons during the burst phase of the inspiratory rhythm.

Inspiratory preBötC neurons receive a large volley of concurrent excitatory synaptic drive from multiple input neurons during each burst (Ashhad and Feldman, 2020). Single-unit recordings from inspiratory neurons (n=10) that were exclusively active during inspiratory bursts were intrinsically quiescent since they did not spike when deprived of excitatory synaptic input. The spiking frequency of inspiratory neurons during bursts was reduced by DAMGO (-37±7%). Similarly, spiking of pre-inspiratory neurons during bursts was reduced by DAMGO (-19±6%). In contrast to the effects on percolation activity, MOR expression did not predict the changes on burst activity, since DAMGO had similar effects on the activity of *Oprm1*+ and *Oprm1*- neurons during bursts (Figure 2G, H). Importantly, these results suggest that any direct effects of MOR activation on the intrinsic excitability of *Oprm1*+ neurons play a minimal role in the suppression of spiking activity during inspiratory bursts.

Network-level effects of MOR activation in the preBötC.

We also explored whether the effects of MOR activation at the cellular level are reflected in corresponding changes at the population level. In horizontal brainstem slices, integrated multi-unit spiking activity was recorded from the preBötC before and during increasing concentrations of DAMGO from 50 to 300 nM. A representative experiment is shown in Figure 3A. As expected

bioRxiv preprint doi: https://doi.org/10.1101/2021.02.24.432816; this version posted February 25, 2021. The copyright holder for this preprint (which was not certified by peer review) is the author/funder, who has granted bioRxiv a license to display the preprint in perpetuity. It is made available under aCC-BY 4.0 International license.

(Gray et al., 1999a, Montandon et al., 2011, Wei and Ramirez, 2019), DAMGO caused a dose-dependent decrease in the frequency of inspiratory bursts, -26±3%, -45+±4%,-63±4% and -74±4% change from baseline in 50, 100, 200, and 300 nM DAMGO, respectively (Figure 3A, C), which did not differ between horizontal slices from heterozygous *Oprm1*$^{Cre/+}$ and wild-type controls (Supplemental Figure 2). The time between inspiratory bursts became more irregular with DAMGO with inconsistent changes in burst-amplitude irregularity (Figure 3C). These hallmarks of OIRD were accompanied by a decrease in the total amount of spiking activity between inspiratory bursts, measured as the integrated inter-burst interval (IBI) amplitude (Figure 3B, C). Integrated IBI spiking was reduced by -12±2%, -15±2%, -17±2% and -18±2% from baseline in 50, 100, 200, and 300 nM DAMGO, respectively (Figure 3C). Changes in burst frequency shared a weak (R^2=0.16) but significant linear relationship with changes in IBI spiking at 100 nM DAMGO (p=0.03) and became progressively less significant with 200 nM (p=0.05) and 300 nM (p=0.08) DAMGO (Supplemental Figure 3). We also noted that many bursts failed to fully form in DAMGO. These failed bursts were characterized by small-amplitude activity occurring in only subsets of the population typically active during successful bursts (Figure 3D, E; Supplemental Figure 4), potentially analogous to “burstlets” (Kam et al., 2013a, Kallurkar et al., 2020). As a fraction of the total burst attempts, such burst failures became more prevalent with increasing concentrations of DAMGO (Figure 3E) with 43±5% of bursts attempts failing in 300 nM DAMGO.

We also examined the effects of systemic MOR activation on preBötC population activity *in vivo*. In urethane-anesthetized, adult mice, rhythmic integrated-spiking activity was recorded from the preBötC while simultaneously recording inspiratory motor output from the XII nerve (Figure 3F). Example preBötC and XII activity under control conditions (baseline) and ~10 min following intraperitoneal morphine (150 mg/kg) are shown in Figure 3G. Changes in total integrated IBI spiking activity before and after morphine are exemplified in Figure 3H. Morphine

bioRxiv preprint doi: https://doi.org/10.1101/2021.02.24.432816; this version posted February 25, 2021. The copyright holder for this preprint (which was not certified by peer review) is the author/funder, who has granted bioRxiv a license to display the preprint in perpetuity. It is made available under aCC-BY 4.0 International license.

significantly reduced the total preBötC spiking activity during the IBI (IBI spiking) by -17±5%. Breathing frequency was also significantly decreased by morphine (-31±6%) (Figure 3I); however, changes in frequency were not related to changes in spiking activity during the IBI (linear regression; $p>0.05$). At the level of the preBötC, changes in frequency were primarily due to a 74±22% increase in the duration of the IBI from 386±84 ms to 629±97 ms along with a comparatively modest 16±3% increase in the duration of preBötC bursts (TI) (258±14 ms to 300±19 ms) due to slower burst-rise times (Figure 3J), consistent with reports of reduced peak inspiratory flow during OIRD (Ferguson and Drummond, 2006).

Hyperpolarization of Oprm1+ preBötC neurons only partially mimics OIRD.

OIRD is often attributed to mechanisms leading to membrane hyperpolarization and reduced spiking activity of respiratory neurons (Liang et al., 2018, Montandon et al., 2016, Montandon and Slutsky, 2019, Montandon et al., 2011). However, we found that IBI spiking of *Oprm1*+ preBötC neurons was suppressed but not silenced during OIRD (see Figure 2). To address if this decrease in spiking activity is sufficient to explain the pronounced decrease in inspiratory frequency that occurs when the preBötC network is challenged with exogenous opioids, we employed optogenetic tools and expressed ArchT, an enhanced light activated outward proton pump, specifically within *Oprm1*+ neurons. This approach allowed us to examine changes in preBötC network function caused by hyperpolarization of *Oprm1*+ neurons.

In horizontal brainstem slices from *Oprm1*^{Cre}; *Rosa*26^{ArchT} mice, rhythmic integrated multi-unit preBötC activity was recorded during 10 s of continuous bilateral pulses of 598 nm light at 2, 4, and 6 mW. Slices were then exposed to 50, 100, 200, or 300 nM DAMGO, and light-pulse trials were repeated (Figure 4A-D). As expected, bilateral hyperpolarization of *Oprm1*+ preBötC neurons (Supplemental Figure 5) suppressed network spiking during the IBI (-

bioRxiv preprint doi: https://doi.org/10.1101/2021.02.24.432816; this version posted February 25, 2021. The copyright holder for this preprint (which was not certified by peer review) is the author/funder, who has granted bioRxiv a license to display the preprint in perpetuity. It is made available under aCC-BY 4.0 International license.

24±3% at 2 mW, -32±4% at 4 mW, and -40±4% at 6 mW). Photoinhibition also depressed the frequency of inspiratory population bursts by -20±7% at 2 mW, -32±10% at 4 mW, and -49±8% at 6 mW; and changes in burst frequency were proportional to the suppression of IBI spiking (burst frequency/IBI spiking ratio: 1.06±0.1 at 2 mW, 1.02±0.16 at 4 mW, and 0.875±0.15 at 6 mW) (Figure 4C). Interestingly, subsequent application of DAMGO resulted in a comparatively small change in IBI spiking (-13±2% at 50 nM, -17±3% at 100 nM, -17±3% at 200 nM, and -20±4% at 300 nM) despite a more potent slowing of inspiratory burst frequency (-34±7% at 50 nM, -56±8% at 100 nM, -72±8% at 200 nM, and -83±5% at 300 nM). Indeed, in response to DAMGO, changes in burst frequency were not proportional to changes in IBI spiking (0.74±0.09 at 50nM, 0.52±0.09 at 100nM, 0.33±0.10 at 200nM, and 0.225±0.08 at 300nM) (Figure 4C). Moreover, at 2mW (but not 4 or 6mW) bilateral photoinhibition of *Oprm1*+ preBötC neurons caused suppressed IBI spiking by an amount equivalent (p=0.42) to 300 nM DAMGO (Figure 4D), yet inspiratory burst frequency was reduced by only -20±7% during photoinhibiton compared to -83±5% in 300 nM DAMGO (Figure 4D). In addition, consistent with our observations from single-unit recordings (see Figure 2), MOR activation by DAMGO only partially suppressed spiking activity of *Oprm1*+ preBötC neurons. Even after the inspiratory population rhythm had been nearly silenced by 300 nM DAMGO, light-mediated hyperpolarization of *Oprm1*+ preBötC neurons continued to reduce IBI spiking by -39±5% at 6 mW (Figure 4C). We conclude that MOR activation causes a significant frequency reduction that is associated with only a small reduction in network spiking activity *in vitro*.

We also tested whether optogenetic suppression of preBötC spiking activity is sufficient to mimic OIRD *in vivo*. PreBötC spiking activity and XII motor output were recorded simultaneously from urethane-anesthetized adult *Oprm1*^{Cre}; *Rosa26*^{ArchT} mice during bilateral photoinhibition of *Oprm1*+ preBötC neurons (Figure 4E). A representative experiment is shown in Figure 4F. We found that 6 mW photoinhibition of *Oprm1*+ preBötC neurons was sufficient to

bioRxiv preprint doi: https://doi.org/10.1101/2021.02.24.432816; this version posted February 25, 2021. The copyright holder for this preprint (which was not certified by peer review) is the author/funder, who has granted bioRxiv a license to display the preprint in perpetuity. It is made available under aCC-BY 4.0 International license.

298 suppress IBI spiking by -20±5%, an amount similar (p=0.72) to changes in IBI spiking induced
299 by morphine administration (Figure 4I). To further examine the cellular consequences of
300 photoinhibition, we recorded single preBötC units *in vivo* during 6-mW light pulses. We found
301 that photoinhibition reduced, but did not eliminate, spiking from most preBötC neurons (Figure
302 4H). However, consistent with our findings *in vitro*, photoinhibition of *Oprm1*+ preBötC neurons
303 did not phenocopy OIRD because breathing frequency was unaffected (-1±5% change). Indeed,
304 changes in breathing frequency and the ratio of burst frequency/IBI spiking induced by morphine
305 administration were significantly different than changes observed during photoinhibition of
306 *Oprm1*+ preBötC neurons (Figure 4I). Taken together, these results suggest that
307 hyperpolarization and reduced spiking of *Oprm1*+ preBötC neurons cannot fully account for
308 OIRD *in vitro* and seems to be even less consequential for OIRD *in vivo*.

309

310 ***Pre-synaptic drive from Oprm1+ preBötC neurons is reduced by MOR activation.***

311 Based on these observations, we wondered what mechanisms may account for the
312 disproportionate frequency effects of exogenous opioids on preBötC rhythmogenesis relative to
313 their effects on the spiking activity of preBötC neurons. The frequency of miniature EPSCs
314 recorded from individual preBötC neurons is reduced by DAMGO (Wei and Ramirez, 2019),
315 suggesting that suppression of synaptic transmission within the preBötC network may contribute
316 to OIRD. To further test this hypothesis, we examined how MOR activation affects evoked
317 EPSPs driven specifically by *Oprm1*+ neurons. We first determined the response characteristics
318 of channelrhodopsin2 expressing *Oprm1*+ preBötC neurons when directly activated by brief light
319 pulses (10 ms, 0.75 mW, ~50 trials for each neuron). All *Oprm1*+ neurons reliably generated a
320 spike (1.13±0.08 spikes/stimulation) with a latency of 9.4±0.6 ms that was consistent among
321 stimulus trials (SD of latency: 1.42±0.22) (Figure 5A, B, C) (Széll et al., 2020). In contrast, only 7
322 of 16 (44%) *Oprm1*- neurons produced spikes in response to light pulses. When compared to

bioRxiv preprint doi: https://doi.org/10.1101/2021.02.24.432816; this version posted February 25, 2021. The copyright holder for this preprint (which was not certified by peer review) is the author/funder, who has granted bioRxiv a license to display the preprint in perpetuity. It is made available under aCC-BY 4.0 International license.

323 *Oprm1*+ neurons, the spikes generated by *Oprm1*- neurons were unreliable (0.24±0.09
324 spikes/stimulation) with a longer latency from light onset (19.2±1.6 ms) and exhibited more jitter
325 from trial to trial (SD of latency: 5.8±1.1).

326 We tested whether activation of *Oprm1*+ neurons would produce corresponding EPSPs
327 in contralateral preBötC neurons via commissural projections, and whether these excitatory
328 interactions are inhibited by MOR activation. Membrane potential was recorded from inspiratory
329 preBötC neurons in whole-cell configuration while delivering light pulses to the contralateral
330 preBötC (Figure 5D). Neurons that received excitatory synaptic input from contralateral *Oprm1*+
331 neurons (n=6 of 30 recorded neurons) were then selected based on the presence of
332 consistently evoked EPSPs following the onset of each light pulse. For each of these *Oprm1*+
333 (n=3) and *Oprm1*- (n=3) neurons, evoked EPSPs were recorded during 50-100 stimulus trials
334 under baseline conditions. Stimulus trials were then repeated in 50 nM and 300 nM DAMGO. In
335 some neurons, a hyperpolarizing holding current was applied to maintain V_m below spiking
336 threshold throughout the experiment. The amplitude of EPSPs evoked by activation of
337 contralateral *Oprm1*+ neurons was reduced by DAMGO (-20±7% and -49±12% in 50 nM and
338 300 nM DAMGO, respectively) (Figure 5E). Notably, evoked EPSP amplitude was similarly
339 reduced in *Oprm1*+ and *Oprm1*- neurons (p=0.6). Collectively, these data indicate that MOR-
340 expressing neurons have commissural projections, and MOR activation suppresses excitatory
341 synaptic transmission from *Oprm1*+ neurons to their postsynaptic targets.

342

343 ***MOR activation limits the ability of Oprm1+ preBötC neurons to drive the inspiratory***
344 ***rhythm.***

345 To test for evidence of impaired synaptic transmission at the population-level, integrated multi-
346 unit preBötC activity was recorded during a strong (0.75 mW) sustained (10 s) photoactivation

bioRxiv preprint doi: https://doi.org/10.1101/2021.02.24.432816; this version posted February 25, 2021. The copyright holder for this preprint (which was not certified by peer review) is the author/funder, who has granted bioRxiv a license to display the preprint in perpetuity. It is made available under aCC-BY 4.0 International license.

of contralateral *Oprm1*+ neurons under baseline conditions and in 300 nM DAMGO (Supplemental Figure 6A). At baseline, photoactivation of *Oprm1*+ neurons (Supplemental Figure 5) caused a 29±6% increase in the total integrated spiking activity in the contralateral preBötC; however, this effect was significantly reduced to 5±2% in the presence of DAMGO (Supplemental Figure 6B). The ability of commissural *Oprm1*+ neurons to drive an increase in inspiratory burst frequency was also reduced by DAMGO (Supplemental Figure 6C). Similar results were observed during bilateral photoactivation *Oprm1*+ preBötC neurons with 20-s continuous light pulses (3-5 trails per light power) (Figure 6A, B). Under baseline conditions, light stimulation produced a robust increase in the frequency of inspiratory bursts (53±6% at 0.05 mW, 99±11% at 0.15 mW, and 131±15% at 0.25 mW) (Figure 6C, D). *Oprm1*+ neuron stimulation also increased network spiking during the IBI (35±4% at 0.05 mW, 81±11% at 0.15 mW, and 95±13% at 0.25 mW). Like the effects of *Oprm1*+ neuron hyperpolarization (see Figure 4), changes in inspiratory burst frequency were proportional to changes in IBI spiking activity (burst frequency/IBI spiking ratio: 1.13±0.05 at 0.05 mW, 1.12±0.07 at 0.15 mW, and 1.21±0.08 at 0.25 mW) (Figure 6C, D). Light pulses were repeated in the presence of 300 nM DAMGO to test how MOR activation may alter the ability of *Oprm1*+ neuron depolarization to regulate network function. In 300 nM DAMGO, inspiratory burst frequency was reduced to 37±6% of baseline levels. Burst frequency could be partially restored by depolarization of *Oprm1*+ preBötC neurons to 61±6%, 87±8%, and 95±9% of baseline levels by 0.05, 0.15, and 0.25 mW, respectively (Figure 6D). Thus, *Oprm1*+ neurons remain functionally integrated within the preBötC network during OIRD. However, the relationship between changes in burst frequency and depolarization of *Oprm1*+ neurons, quantified as a slope (Hz/mW), was reduced by DAMGO (0.44±0.05 Hz/mW at baseline vs. 0.21±0.02 Hz/mW in DAMGO; p=0.0004) (Figure 6E). In contrast, following MOR activation, changes in the amount of network-spiking activity elicited by *Oprm1*+ neuron depolarization (17±12% at 0.05 mW, 57±12% at 0.15 mW, and 77±15% at 0.25 mW) were not different from baseline conditions. Indeed, DAMGO did not alter

bioRxiv preprint doi: https://doi.org/10.1101/2021.02.24.432816; this version posted February 25, 2021. The copyright holder for this preprint (which was not certified by peer review) is the author/funder, who has granted bioRxiv a license to display the preprint in perpetuity. It is made available under aCC-BY 4.0 International license.

the relationship between changes in network spiking and depolarization of *Oprm1*+ neurons (Slope: 1.32±0.19 IBI spiking/mW at baseline and 1.23±0.15 IBI spiking/mW in 300 nM DAMGO) (Figure 6E), suggesting the ability of *Oprm1*+ preBötC neurons to spike when depolarized is not impaired by pharmacological MOR activation. The relationship between changes in network spiking and inspiratory frequency remained proportional in DAMGO (burst frequency/IBI spiking ratio: 0.61±0.13 at 0.05 mW 0.59±0.07 at 0.15 mW 0.57±0.06 at 0.25 mW) (Figure 6D). However, the relationship was shifted such that larger changes in spiking activity were needed to produce the same change in inspiratory burst frequency. For example, although depolarization of *Oprm1*+ preBötC neurons could restore inspiratory burst frequency to ~95% of baseline at the highest light power tested, this required an ~80% increase in network spiking above baseline levels. Consistent with these results in brainstems slices, we found that bilateral photoactivation of *Oprm1*+ preBötC neurons *in vivo* increased IBI spiking (Figure 6F, G, H) and produced a light power-dependent increase in breathing frequency (14±7% at 0.05 mW, 29±8% at 0.15 mW, and 39±8% at 0.25 mW). Following morphine administration (150 mg/kg *i.p.*), photoactivation of *Oprm1*+ preBötC neurons continued to increase breathing frequency (Figure 6I, J), but to a lesser extent and with less light power-dependence (0.53±0.1 Hz/mW at baseline vs. 0.18±0.05 Hz/mW in DAMGO) (Figure 6J, K). Collectively, these data suggest that MOR activation causes the spiking activity of *Oprm1*+ preBötC neurons to become less consequential for preBötC network function.

Modelling the functional consequences of preBötC MOR activation in silico.

Based on the experimental results *in vitro* and *in vivo* described above, we constructed a computational network *in silico* to model the effects of MOR activation on preBötC rhythmogenesis. Our model network, based on elements from prior preBötC computational studies (Butera et al., 1999a, Butera et al., 1999b, Park and Rubin, 2013, Harris et al., 2017),

bioRxiv preprint doi: https://doi.org/10.1101/2021.02.24.432816; this version posted February 25, 2021. The copyright holder for this preprint (which was not certified by peer review) is the author/funder, who has granted bioRxiv a license to display the preprint in perpetuity. It is made available under aCC-BY 4.0 International license.

contains 300 total model neurons, 80% designated as excitatory and 20% inhibitory, connected randomly with an average of 6 connections/neuron. The intrinsic spiking activity (i.e., without synaptic interactions) of the model neurons was set such that 65% were quiescent (Q) and 35% exhibited tonic spiking (T). Specific conductance parameters for each model neuron type are summarized in Supplementary Table 1 and described in Methods. Based on our optogenetic-tagging experiments *in vitro* (see Figure 1), we introduced the dynamic parameters I_{opioid} and syn_{opioid} to a subpopulation of *Oprm1*+ neurons, encompassing 50% of all excitatory model neurons. I_{opioid} introduces a hyperpolarizing current to the subpopulation of *Oprm1*+ model neurons (Figure 7B), whereas syn_{opioid} reduces the strength of synaptic output (i.e., pre-synaptic) from *Oprm1*+ neurons. With these parameters set to 0 (i.e., under control conditions), the model preBötC network produced robust rhythmic bursting activity like preBötC rhythms *in vitro* (Figure 7C).

To test the functional role of the modelled *Oprm1*+ subpopulation, *Oprm1*+ neurons were removed from the rhythmogenic process by either 1) increasing I_{opioid} such that spikes were no longer generated by *Oprm1*+ neurons, or 2) increasing syn_{opioid} such that the spikes produced by *Oprm1*+ neurons were inconsequential for their postsynaptic targets (Supplemental Figure 7). Consistent with the critical role of *Oprm1*+ neurons for preBötC rhythmogenesis *in vitro* (Bachmutsky et al., 2020, Gray et al., 1999a, Montandon et al., 2011, Wei and Ramirez, 2019, Mellen et al., 2003), both methods of functionally removing the modelled *Oprm1*+ subpopulation effectively silenced the network rhythm. It is noteworthy, however, that hyperpolarizing *Oprm1*+ model neurons vs. blocking their synaptic output had distinct effects on spiking activity generated by the network, reminiscent of the differential effects on network spiking we observed during optogenetic hyperpolarization of *Oprm1*+ neurons vs. MOR activation (see Figure 4).

bioRxiv preprint doi: https://doi.org/10.1101/2021.02.24.432816; this version posted February 25, 2021. The copyright holder for this preprint (which was not certified by peer review) is the author/funder, who has granted bioRxiv a license to display the preprint in perpetuity. It is made available under aCC-BY 4.0 International license.

We utilized our computational model network to dissociate the functional consequences of the intrinsic vs. synaptic effects of preBötC MOR activation by manipulating I_{opioid} and syn_{opioid} independently or in combination (Figure 7D; Supplemental Figure 8). Each combination of I_{opioid} and syn_{opioid} was repeated over n=8 unique synaptic connectivity patterns. I_{opioid} was varied from 0pA to 6pA, which was more than sufficient to strongly suppress the IBI spiking of intrinsically tonic (T) *Oprm1*+ model neurons (Supplemental Figure 8), consistent with the effects of 300 nM DAMGO *in vitro* (see Figure 2). Syn_{opioid} was varied from 0 to 0.6 (i.e. synaptic strength=100% to 40% of baseline), since this value range was sufficient to account for on our *in vitro* data demonstrating that 300 nM DAMGO suppresses the amplitude of EPSPs driven by *Oprm1*+ neurons by ~50% (see Figure 5D,E). When varying I_{opioid} and syn_{opioid} independently, we found that neither parameter reliably reproduced the effects of MOR activation in the preBötC. Indeed, as I_{opioid} was increased, burst frequency was only moderately reduced. As synaptic efficacy decreased, burst amplitude was reduced with inconsistent effects on burst frequency and irregularity. In contrast, manipulation of I_{opioid} and syn_{opioid} in combination had consequences for the model network rhythm that were surprisingly like the effects of MOR activation in the preBötC (Figure 7C, D). Frequency was reduced, IBI irregularity was increased, and periodic burst failures became apparent (Figure 7C). The model network responded similarly to simulated MOR activation with synaptic inhibition blocked (Figure 7C, D), consistent with experimental observations suggesting that inhibitory mechanisms do not play a significant role in producing OIRD (Bachmutsky et al., 2020, Gray et al., 1999a).These network-level effects of simulated MOR activation were associated with changes in the spiking activity of model neurons that were also consistent with our experimental results. Specifically, changes in spiking activity occurred primarily during the inter-burst interval, due to a preferential suppression of spiking among *Oprm1*+ vs. *Oprm1*- intrinsically tonic (T) neurons (Figure 7E, F), whereas spiking during inspiratory bursts was reduced similarly among *Oprm1*+ and *Oprm1*- model neurons (Figure 7G). These results *in silico* support important, yet interdependent, roles for both intrinsic and

bioRxiv preprint doi: https://doi.org/10.1101/2021.02.24.432816; this version posted February 25, 2021. The copyright holder for this preprint (which was not certified by peer review) is the author/funder, who has granted bioRxiv a license to display the preprint in perpetuity. It is made available under aCC-BY 4.0 International license.

448 synaptic mechanisms underlying MOR-mediated suppression of rhythmogenesis in the
449 preBötC.

450

451 ## Discussion

452 OIRD is a life threating consequence of clinical and illicit opioid use that stems from the high
453 sensitivity of the respiratory control network to MOR activation. Developing a detailed
454 mechanistic understanding of how opioids disturb rhythmogenesis at the cellular and network
455 level will help facilitate the development of new strategies to protect against and reverse OIRD.
456 In this study, we show that MOR activation among a subset of *Oprm1*+ neurons reduces the
457 number of spikes, while also impairing the ability of each spike to drive synaptic transmission,
458 thereby functionally dis-integrating *Oprm1*+ neurons from the recurrently connected preBötC
459 network. We propose that these dual consequences of MOR activation in the preBötC
460 undermine the generally robust nature of the respiratory rhythm, making it particularly
461 vulnerable to exogenous opioids.

462 Breathing must be integrated with complex volitional and reflexive behaviors including
463 vocalization, feeding, sensory exploration, and exercise. As such, the inspiratory-rhythm-
464 generating network must be assembled in a way that allows it to be extremely flexible yet
465 reliable in order to reconcile these complex behaviors with the inexorable physiological
466 requirement for gas exchange. At the core of this network, is the preBötC (Baertsch et al., 2019,
467 Smith et al., 1991b). The preBötC contains an intermingled population of neurons with
468 heterogeneous gene expression and connectomes that interact to produce distinct firing
469 phenotypes or “discharge identities” (Segers et al., 2012, Lalley and Mifflin, 2017, Baertsch et
470 al., 2018). Collectively, this spiking activity results in a rhythmogenic process that can be divided
471 into three functionally distinct phases: a refractory phase, a percolation phase, and a burst
472 phase. Each phase of the inspiratory rhythm can be differentially regulated by neuromodulators

bioRxiv preprint doi: https://doi.org/10.1101/2021.02.24.432816; this version posted February 25, 2021. The copyright holder for this preprint (which was not certified by peer review) is the author/funder, who has granted bioRxiv a license to display the preprint in perpetuity. It is made available under aCC-BY 4.0 International license.

(Baertsch and Ramirez, 2019) or synaptic inputs (Zuperku et al., 2019) to drive dynamic changes in the frequency and regularity of inspiration. For example, the excitatory neuromodulator and potent respiratory stimulant, substance P (SP), specifically affects the percolation phase of the rhythm by increasing the spiking activity of pre-inspiratory neurons between, but not during, bursts. This phase-specific change in spiking activity reduces the time and variability of the IBI, leading to a faster and more regular inspiratory rhythm (Baertsch and Ramirez, 2019).

Here we explored this concept in the context of OIRD. Based on single-unit recordings, we find that ~50% of functionally identified preBötC neurons express the *Oprm1* gene, consistent with expression patterns of *Oprm1* determined by ISH (Allen Brain Atlas; Supplemental Figure 1) and transgenic mice with a fluorescent reporter fused to the MOR (Erbs et al., 2015). Our single-unit recordings also indicate that *Oprm1* expression is evenly distributed among preBötC neuron discharge identities, including putatively rhythmogenic pre-inspiratory neurons (Ashhad and Feldman, 2020, Del Negro et al., 2010, Kam et al., 2013a). Indeed, *Oprm1*-expressing neurons are critical for preBötC rhythmogenesis since pharmacological MOR activation in this isolated network can cause cessation of the rhythm (Bachmutsky et al., 2020, Gray et al., 1999a, Montandon et al., 2011, Wei and Ramirez, 2019, Mellen et al., 2003). Perhaps surprisingly, our data indicate that opioid concentrations that are sufficient to induce severe OIRD did not silence *Oprm1*+ preBötC neurons but reduced spiking activity of pre-inspiratory neurons preferentially during the period between inspirations. These opioid-induced changes in spiking activity were related to each individual neuron's intrinsic activity when deprived of synaptic inputs. Surprisingly, most pre-inspiratory neurons intrinsically produced tonic spiking activity in the absence of excitatory synaptic input. This is notable because it suggests that for these neurons the pre-inspiratory ramp pattern is primarily driven by recovery from intrinsic refractory properties (Baertsch et al., 2018, Krey et al., 2010) rather than

bioRxiv preprint doi: https://doi.org/10.1101/2021.02.24.432816; this version posted February 25, 2021. The copyright holder for this preprint (which was not certified by peer review) is the author/funder, who has granted bioRxiv a license to display the preprint in perpetuity. It is made available under aCC-BY 4.0 International license.

mechanisms of recurrent synaptic excitation. Consistent with the pre-inspiratory spiking activity of these neurons being driven by intrinsic mechanisms, we found that MOR activation had a much greater effect on pre-inspiratory spiking of *Oprm1*+ vs *Oprm1*- intrinsically tonic neurons (Figure 2D). In contrast, among intrinsically quiescent neurons where excitatory synaptic input is the primary driver of pre-inspiratory spiking, MOR activation produced a substantial suppression of pre-inspiratory spiking regardless of *Oprm1* expression (Figure 2F). Thus, OIRD involves reduced spiking during the percolation phase due, in part, to suppression of intrinsically driven pre-inspiratory spiking of *Oprm1*+ neurons and de-recruitment of neurons with synaptically driven, pre-inspiratory spiking activity. Thus, we predict that opioid-induced suppression of preBötC activity during the percolation phase underlies the prolonged and irregular durations between inspiratory efforts that are characteristic of OIRD in both mice and humans (Walker et al., 2007, Wu et al., 2020, Varga et al., 2020).

These effects on preBötC spiking activity are largely opposite to those produced by the respiratory stimulant SP (Baertsch and Ramirez, 2019) and, interestingly, MOR activation can inhibit the release of SP in the spinal cord (Chen et al., 2018). Yet, SP only partially reverses OIRD in brainstem slices (Sun et al., 2019). The preferential suppression of intrinsically driven IBI spiking we observed among *Oprm1*+ pre-inspiratory neurons (Figure 2) is consistent with opioids causing hyperpolarization of MOR-expressing neurons (Gray et al., 1999b, Montandon et al., 2011). However, mimicking changes in preBötC spiking activity during OIRD via hyperpolarization of *Oprm1*+ preBötC neurons causes only a moderate suppression of the inspiratory rhythm *in vitro* and is even less consequential *in vivo* (Figure 4), suggesting that additional mechanisms play an important role (Ren et al., 2019, Wei and Ramirez, 2019, Akins and McCleskey, 1993). Indeed, we find the effects of exogenous opioids in the preBötC go beyond changes in spiking activity. MOR activation also weakened excitatory synaptic connections (Figure 5D, E), like effects on spinal nociceptive pre-synaptic terminals (Corder et

bioRxiv preprint doi: https://doi.org/10.1101/2021.02.24.432816; this version posted February 25, 2021. The copyright holder for this preprint (which was not certified by peer review) is the author/funder, who has granted bioRxiv a license to display the preprint in perpetuity. It is made available under aCC-BY 4.0 International license.

al., 2017). As a result, the remaining spiking activity of *Oprm1*+ preBötC neurons becomes less consequential for network function (Figure 6). Thus, considering the recurrent connectivity within the preBötC (Guerrier et al., 2015, Rubin et al., 2009, Yang and Feldman, 2018, Yang et al., 2020), it is not surprising that the suppressive effect of opioids on synaptically driven pre-inspiratory spiking is not specific to MOR-expressing preBötC neurons (Figure 2E, 5E). Importantly, the efficacy of spiking activity could not be restored by depolarizing *Oprm1*+ preBötC neurons, suggesting the pre-synaptic effect of MOR activation in the preBötC is independent from changes in membrane potential. These results help explain mechanistically the effectiveness of ampakines for reversing OIRD (Ren et al., 2009, Ren et al., 2015, Lorier et al., 2010, Greer and Ren, 2009), because potentiation of post-synaptic AMPAR currents could compensate for opioid-induced impairments in excitatory pre-synaptic transmission. However, ampakine treatment would not be expected to reverse the intrinsic hyperpolarizing effect of opioids on *Oprm1*+ preBötC neurons, which could underlie the limitations for ampakine-mediated prevention of OIRD seen clinically (van der Schier et al., 2014, Oertel et al., 2010). Thus, combination therapies that help the inspiratory rhythm generating network compensate for both the intrinsic and synaptic consequences of MOR activation in the preBötC may prove to be a more effective strategy for the prevention and reversal of OIRD without affecting analgesia.

MOR activation also caused a moderate reduction in spiking activity during inspiratory bursts. Because preBötC neurons receive strong synchronized excitatory synaptic input during inspiratory bursts (Ashhad and Feldman, 2020), we suspect that the reduced spike frequency during bursts is primarily due to the suppressive effect of opioids on pre-synaptic transmission (Figure 5D, E). Indeed, spiking of *Oprm1*+ and *Opmr1*- neurons during inspiration was similarly reduced by DAMGO (Figure 2G, H), suggesting that direct effects of MOR activation on the intrinsic excitability of *Oprm1*+ neurons plays a minimal role. Suppressed spiking of single preBötC neurons during inspiratory bursts due to impaired synaptic communication may also

bioRxiv preprint doi: https://doi.org/10.1101/2021.02.24.432816; this version posted February 25, 2021. The copyright holder for this preprint (which was not certified by peer review) is the author/funder, who has granted bioRxiv a license to display the preprint in perpetuity. It is made available under aCC-BY 4.0 International license.

548 contribute to changes in the rate of burst onset observed at the network-level following MOR
549 activation *in vivo* (Figure 3J) (Ferguson and Drummond, 2006) and/or the higher proportion of
550 failed bursts observed *in vitro* (Figure 3D,E). As observed following chronic exposure to
551 intermittent hypoxia (CIH), weakened preBötC activity during the burst phase can lead to
552 periodic and "all or none" type failures of inspiratory drive to be transmitted to the XII motor pool
553 (Garcia et al., 2019, Garcia et al., 2017, Garcia et al., 2016). Indeed, MOR activation reduces
554 inspiratory synaptic drive to XII motor neurons without changing their membrane input
555 resistance and this effect is reversed by ampakines (Lorier et al., 2010), consistent with
556 impaired pre-synaptic transmission in *Oprm1*+ preBötC neurons (Figure 5D, E). Because XII
557 output is important for maintaining upper airway patency, this may have important implications
558 in the context of sleep apnea, which is highly prevalent among opioid users (Mogri et al., 2009,
559 Rose et al., 2014, Walker et al., 2007). Thus, we speculate that the risk of OIRD is amplified by
560 a dangerous feed-forward process that arises due to the synergy between opioids, sleep apnea,
561 and CIH (Lam et al., 2016, Overdyk et al., 2014).

562 Our collective results indicate that only ~50% of preBötC neurons express the *Oprm1*
563 gene and are therefore able to play a direct role in OIRD. Yet, respiratory rhythmogenesis is
564 effectively inhibited, because opioids act with a "double-edged sword" to functionally remove
565 *Oprm1* neurons from the preBötC network. By simultaneously reducing intrinsic excitability and
566 impairing excitatory synaptic communication, exogenous opioids effectively disable the normally
567 robust inspiratory network, leading to long and variable pauses between breaths and ultimately
568 cessation of rhythmogenesis altogether. Thus, interesting, yet unresolved, questions are: Why
569 do these critical rhythm generating neurons express the MOR? Are there circumstances when
570 the heightened opioid sensitivity of the preBötC may provide and evolutionary advantage? And
571 how and when might endogenous opioid signaling play important functional roles in the
572 preBötC? Addressing these important questions may reveal naturally occurring mechanisms or

bioRxiv preprint doi: https://doi.org/10.1101/2021.02.24.432816; this version posted February 25, 2021. The copyright holder for this preprint (which was not certified by peer review) is the author/funder, who has granted bioRxiv a license to display the preprint in perpetuity. It is made available under aCC-BY 4.0 International license.

573 neuromodulatory states that protect this vital respiratory network. Such insights will be a critical
574 next step in the development of novel strategies to protect against and reverse OIRD.

575

576 ## Competing Interests

577 The authors declare no conflicts of interest financial or otherwise.

578

579 ## Acknowledgments

580 We thank Dr. Richard Palmiter and his lab for the development and generous donation of the
581 *Oprm1*$^{Cre:GFP}$ mouse line, Dr. Aguan Wei for helpful edits on the manuscript, and the National
582 Heart, Lung, and Blood Institute for funding this work: K99HL145004 (NAB), R01HL144801
583 (JMR), and F32HL154558 (NJB).

584

585

586

587

588

589

590

591

592

593

594

bioRxiv preprint doi: https://doi.org/10.1101/2021.02.24.432816; this version posted February 25, 2021. The copyright holder for this preprint (which was not certified by peer review) is the author/funder, who has granted bioRxiv a license to display the preprint in perpetuity. It is made available under aCC-BY 4.0 International license.

References

AKINS, P. T. & MCCLESKEY, E. W. 1993. Characterization of potassium currents in adult rat sensory neurons and modulation by opioids and cyclic AMP. Neuroscience, 56, 759-69.

ALGERA, M. H., KAMP, J., VAN DER SCHRIER, R., VAN VELZEN, M., NIESTERS, M., AARTS, L., DAHAN, A. & OLOFSEN, E. 2019. Opioid-induced respiratory depression in humans: a review of pharmacokinetic-pharmacodynamic modelling of reversal. Br J Anaesth, 122, e168-e179.

ASHHAD, S. & FELDMAN, J. L. 2020. Emergent Elements of Inspiratory Rhythmogenesis: Network Synchronization and Synchrony Propagation. Neuron, 106, 482-497.e4.

BACHMUTSKY, I., WEI, X. P., KISH, E. & YACKLE, K. 2020. Opioids depress breathing through two small brainstem sites. Elife, 9.

BAERTSCH, N. A., BAERTSCH, H. C. & RAMIREZ, J. M. 2018. The interdependence of excitation and inhibition for the control of dynamic breathing rhythms. Nat Commun, 9, 843.

BAERTSCH, N. A. & RAMIREZ, J. M. 2019. Insights into the dynamic control of breathing revealed through cell-type-specific responses to substance P. Elife, 8.

BAERTSCH, N. A., SEVERS, L. J., ANDERSON, T. M. & RAMIREZ, J. M. 2019. A spatially dynamic network underlies the generation of inspiratory behaviors. Proc Natl Acad Sci U S A, 116, 7493-7502.

BOUILLON, T., BRUHN, J., ROEPCKE, H. & HOEFT, A. 2003. Opioid-induced respiratory depression is associated with increased tidal volume variability. Eur J Anaesthesiol, 20, 127-33.

BUTERA, R. J., JR., RINZEL, J. & SMITH, J. C. 1999a. Models of respiratory rhythm generation in the pre-Bötzinger complex. I. Bursting pacemaker neurons. J Neurophysiol, 82, 382-97.

BUTERA, R. J., JR., RINZEL, J. & SMITH, J. C. 1999b. Models of respiratory rhythm generation in the pre-Bötzinger complex. II. Populations Of coupled pacemaker neurons. J Neurophysiol, 82, 398-415.

CHEN, W., ENNES, H. S., MCROBERTS, J. A. & MARVIZÓN, J. C. 2018. Mechanisms of μ-opioid receptor inhibition of NMDA receptor-induced substance P release in the rat spinal cord. Neuropharmacology, 128, 255-268.

CONIBEAR, A. E. & KELLY, E. 2019. A Biased View of μ-Opioid Receptors? Mol Pharmacol, 96, 542-549.

CORDER, G., TAWFIK, V. L., WANG, D., SYPEK, E. I., LOW, S. A., DICKINSON, J. R., SOTOUDEH, C., CLARK, J. D., BARRES, B. A., BOHLEN, C. J. & SCHERRER, G. 2017. Loss of μ opioid receptor signaling in nociceptors, but not microglia, abrogates morphine tolerance without disrupting analgesia. Nat Med, 23, 164-173.

DAHAN, A., AARTS, L. & SMITH, T. W. 2010. Incidence, Reversal, and Prevention of Opioid-induced Respiratory Depression. Anesthesiology, 112, 226-38.

bioRxiv preprint doi: https://doi.org/10.1101/2021.02.24.432816; this version posted February 25, 2021. The copyright holder for this preprint (which was not certified by peer review) is the author/funder, who has granted bioRxiv a license to display the preprint in perpetuity. It is made available under aCC-BY 4.0 International license.

631 DAHAN, A., SARTON, E., TEPPEMA, L., OLIEVIER, C., NIEUWENHUIJS, D., MATTHES, H.
632 W. & KIEFFER, B. L. 2001. Anesthetic potency and influence of morphine and sevoflurane on
633 respiration in mu-opioid receptor knockout mice. Anesthesiology, 94, 824-32.

634 DAHAN, A., VAN DER SCHRIER, R., SMITH, T., AARTS, L., VAN VELZEN, M. & NIESTERS,
635 M. 2018. Averting Opioid-induced Respiratory Depression without Affecting Analgesia.
636 Anesthesiology, 128, 1027-1037.

637 DAI, W., XIAO, D., GAO, X., ZHOU, X. B., FANG, T. Y., YONG, Z. & SU, R. B. 2017. A brain-
638 targeted ampakine compound protects against opioid-induced respiratory depression. Eur J
639 Pharmacol, 809, 122-129.

640 DEL NEGRO, C. A., FUNK, G. D. & FELDMAN, J. L. 2018. Breathing matters. Nat Rev
641 Neurosci, 19, 351-367.

642 DEL NEGRO, C. A. & HAYES, J. A. 2008. A 'group pacemaker' mechanism for respiratory
643 rhythm generation. J Physiol, 586, 2245-6.

644 DEL NEGRO, C. A., HAYES, J. A., PACE, R. W., BRUSH, B. R., TERUYAMA, R. & FELDMAN,
645 J. L. 2010. Synaptically activated burst-generating conductances may underlie a group-
646 pacemaker mechanism for respiratory rhythm generation in mammals. Prog Brain Res, 187,
647 111-36.

648 DEL NEGRO, C. A., HAYES, J. A. & REKLING, J. C. 2011. Dendritic calcium activity precedes
649 inspiratory bursts in preBotzinger complex neurons. J Neurosci, 31, 1017-22.

650 DRUMMOND, G. B. 1983. Comparison of decreases in ventilation caused by enflurane and
651 fentanyl during anaesthesia. Br J Anaesth, 55, 825-35.

652 ERBS, E., FAGET, L., SCHERRER, G., MATIFAS, A., FILLIOL, D., VONESCH, J. L., KOCH,
653 M., KESSLER, P., HENTSCH, D., BIRLING, M. C., KOUTSOURAKIS, M., VASSEUR, L.,
654 VEINANTE, P., KIEFFER, B. L. & MASSOTTE, D. 2015. A mu-delta opioid receptor brain atlas
655 reveals neuronal co-occurrence in subcortical networks. Brain Struct Funct, 220, 677-702.

656 FERGUSON, L. M. & DRUMMOND, G. B. 2006. Acute effects of fentanyl on breathing pattern
657 in anaesthetized subjects. Br J Anaesth, 96, 384-90.

658 FUNK, G. D., SMITH, J. C. & FELDMAN, J. L. 1993. Generation and transmission of respiratory
659 oscillations in medullary slices: role of excitatory amino acids. J Neurophysiol, 70, 1497-515.

660 GAL, T. J. 1989. Naloxone reversal of buprenorphine-induced respiratory depression. Clin
661 Pharmacol Ther, 45, 66-71.

662 GARCIA, A. J., 3RD, DASHEVSKIY, T., KHUU, M. A. & RAMIREZ, J. M. 2017. Chronic
663 Intermittent Hypoxia Differentially Impacts Different States of Inspiratory Activity at the Level of
664 the preBötzinger Complex. Front Physiol, 8, 571.

665 GARCIA, A. J., 3RD, VIEMARI, J. C. & KHUU, M. A. 2019. Respiratory rhythm generation,
666 hypoxia, and oxidative stress-Implications for development. Respir Physiol Neurobiol, 270,
667 103259.

bioRxiv preprint doi: https://doi.org/10.1101/2021.02.24.432816; this version posted February 25, 2021. The copyright holder for this preprint (which was not certified by peer review) is the author/funder, who has granted bioRxiv a license to display the preprint in perpetuity. It is made available under aCC-BY 4.0 International license.

668 GARCIA, A. J., 3RD, ZANELLA, S., DASHEVSKIY, T., KHAN, S. A., KHUU, M. A.,
669 PRABHAKAR, N. R. & RAMIREZ, J. M. 2016. Chronic Intermittent Hypoxia Alters Local
670 Respiratory Circuit Function at the Level of the preBötzinger Complex. Front Neurosci, 10, 4.

671 GRAY, P. A., REKLING, J. C., BOCCHIARO, C. M. & FELDMAN, J. L. 1999a. Modulation of
672 respiratory frequency by peptidergic input to rhythmogenic neurons in the preBotzinger
673 complex. Science, 286, 1566-8.

674 GRAY, P. A., REKLING, J. C., BOCCHIARO, C. M. & FELDMAN, J. L. 1999b. Modulation of
675 respiratory frequency by peptidergic input to rhythmogenic neurons in the preBötzinger
676 complex. Science, 286, 1566-8.

677 GREER, J. J. & REN, J. 2009. Ampakine therapy to counter fentanyl-induced respiratory
678 depression. Respir Physiol Neurobiol, 168, 153-7.

679 GREER, J. J., SMITH, J. C. & FELDMAN, J. L. 1991. Role of excitatory amino acids in the
680 generation and transmission of respiratory drive in neonatal rat. J Physiol, 437, 727-49.

681 GUENTHER, U., WRIGGE, H., THEUERKAUF, N., BOETTCHER, M. F., WENSING, G.,
682 ZINSERLING, J., PUTENSEN, C. & HOEFT, A. 2010. Repinotan, a selective 5-HT1A-R-agonist,
683 antagonizes morphine-induced ventilatory depression in anesthetized rats. Anesth Analg, 111,
684 901-7.

685 GUERRIER, C., HAYES, J. A., FORTIN, G. & HOLCMAN, D. 2015. Robust network oscillations
686 during mammalian respiratory rhythm generation driven by synaptic dynamics. Proc Natl Acad
687 Sci U S A, 112, 9728-33.

688 GUPTA, K., PRASAD, A., NAGAPPA, M., WONG, J., ABRAHAMYAN, L. & CHUNG, F. F. 2018.
689 Risk factors for opioid-induced respiratory depression and failure to rescue: a review. Curr Opin
690 Anaesthesiol, 31, 110-119.

691 HARRIS, K. D., DASHEVSKIY, T., MENDOZA, J., GARCIA, A. J., 3RD, RAMIREZ, J. M. &
692 SHEA-BROWN, E. 2017. Different roles for inhibition in the rhythm-generating respiratory
693 network. J Neurophysiol, 118, 2070-2088.

694 HAW, A. J., MEYER, L. C., GREER, J. J. & FULLER, A. 2016. Ampakine CX1942 attenuates
695 opioid-induced respiratory depression and corrects the hypoxaemic effects of etorphine in
696 immobilized goats (Capra hircus). Vet Anaesth Analg, 43, 528-38.

697 IMAM, M. Z., KUO, A. & SMITH, M. T. 2020. Countering opioid-induced respiratory depression
698 by non-opioids that are respiratory stimulants. F1000Res, 9.

699 KALLURKAR, P. S., GROVER, C., PICARDO, M. C. D. & DEL NEGRO, C. A. 2020. Evaluating
700 the Burstlet Theory of Inspiratory Rhythm and Pattern Generation. eNeuro, 7.

701 KAM, K., WORRELL, J. W., JANCZEWSKI, W. A., CUI, Y. & FELDMAN, J. L. 2013a. Distinct
702 inspiratory rhythm and pattern generating mechanisms in the preBotzinger complex. J Neurosci,
703 33, 9235-45.

704 KAM, K., WORRELL, J. W., VENTALON, C., EMILIANI, V. & FELDMAN, J. L. 2013b.
705 Emergence of population bursts from simultaneous activation of small subsets of preBotzinger
706 complex inspiratory neurons. J Neurosci, 33, 3332-8.

bioRxiv preprint doi: https://doi.org/10.1101/2021.02.24.432816; this version posted February 25, 2021. The copyright holder for this preprint (which was not certified by peer review) is the author/funder, who has granted bioRxiv a license to display the preprint in perpetuity. It is made available under aCC-BY 4.0 International license.

KIMURA, S., OHI, Y. & HAJI, A. 2015. Blockade of phosphodiesterase 4 reverses morphine-induced ventilatory disturbance without loss of analgesia. Life Sci, 127, 32-8.

KIRBY, G. C. & MCQUEEN, D. S. 1986. Characterization of opioid receptors in the cat carotid body involved in chemosensory depression in vivo. Br J Pharmacol, 88, 889-98.

KLIEWER, A., GILLIS, A., HILL, R., SCHMIEDEL, F., BAILEY, C., KELLY, E., HENDERSON, G., CHRISTIE, M. J. & SCHULZ, S. 2020. Morphine-induced respiratory depression is independent of β-arrestin2 signalling. Br J Pharmacol, 177, 2923-2931.

KLIEWER, A., SCHMIEDEL, F., SIANATI, S., BAILEY, A., BATEMAN, J. T., LEVITT, E. S., WILLIAMS, J. T., CHRISTIE, M. J. & SCHULZ, S. 2019. Phosphorylation-deficient G-protein-biased μ-opioid receptors improve analgesia and diminish tolerance but worsen opioid side effects. Nat Commun, 10, 367.

KOTTICK, A. & DEL NEGRO, C. A. 2015. Synaptic Depression Influences Inspiratory-Expiratory Phase Transition in Dbx1 Interneurons of the preBotzinger Complex in Neonatal Mice. J Neurosci, 35, 11606-11.

KREY, R. A., GOODREAU, A. M., ARNOLD, T. B. & DEL NEGRO, C. A. 2010. Outward Currents Contributing to Inspiratory Burst Termination in preBötzinger Complex Neurons of Neonatal Mice Studied in Vitro. Front Neural Circuits, 4, 124.

LALLEY, P. M. & MIFFLIN, S. W. 2017. Oscillation patterns are enhanced and firing threshold is lowered in medullary respiratory neuron discharges by threshold doses of a μ-opioid receptor agonist. Am J Physiol Regul Integr Comp Physiol, 312, R727-r738.

LAM, K. K., KUNDER, S., WONG, J., DOUFAS, A. G. & CHUNG, F. 2016. Obstructive sleep apnea, pain, and opioids: is the riddle solved? Curr Opin Anaesthesiol, 29, 134-40.

LEIN, E. S., HAWRYLYCZ, M. J., AO, N., AYRES, M., BENSINGER, A., BERNARD, A., BOE, A. F., BOGUSKI, M. S., BROCKWAY, K. S., BYRNES, E. J., CHEN, L., CHEN, L., CHEN, T. M., CHIN, M. C., CHONG, J., CROOK, B. E., CZAPLINSKA, A., DANG, C. N., DATTA, S., DEE, N. R., DESAKI, A. L., DESTA, T., DIEP, E., DOLBEARE, T. A., DONELAN, M. J., DONG, H. W., DOUGHERTY, J. G., DUNCAN, B. J., EBBERT, A. J., EICHELE, G., ESTIN, L. K., FABER, C., FACER, B. A., FIELDS, R., FISCHER, S. R., FLISS, T. P., FRENSLEY, C., GATES, S. N., GLATTFELDER, K. J., HALVERSON, K. R., HART, M. R., HOHMANN, J. G., HOWELL, M. P., JEUNG, D. P., JOHNSON, R. A., KARR, P. T., KAWAL, R., KIDNEY, J. M., KNAPIK, R. H., KUAN, C. L., LAKE, J. H., LARAMEE, A. R., LARSEN, K. D., LAU, C., LEMON, T. A., LIANG, A. J., LIU, Y., LUONG, L. T., MICHAELS, J., MORGAN, J. J., MORGAN, R. J., MORTRUD, M. T., MOSQUEDA, N. F., NG, L. L., NG, R., ORTA, G. J., OVERLY, C. C., PAK, T. H., PARRY, S. E., PATHAK, S. D., PEARSON, O. C., PUCHALSKI, R. B., RILEY, Z. L., ROCKETT, H. R., ROWLAND, S. A., ROYALL, J. J., RUIZ, M. J., SARNO, N. R., SCHAFFNIT, K., SHAPOVALOVA, N. V., SIVISAY, T., SLAUGHTERBECK, C. R., SMITH, S. C., SMITH, K. A., SMITH, B. I., SODT, A. J., STEWART, N. N., STUMPF, K. R., SUNKIN, S. M., SUTRAM, M., TAM, A., TEEMER, C. D., THALLER, C., THOMPSON, C. L., VARNAM, L. R., VISEL, A., WHITLOCK, R. M., WOHNOUTKA, P. E., WOLKEY, C. K., WONG, V. Y., et al. 2007. Genome-wide atlas of gene expression in the adult mouse brain. Nature, 445, 168-76.

bioRxiv preprint doi: https://doi.org/10.1101/2021.02.24.432816; this version posted February 25, 2021. The copyright holder for this preprint (which was not certified by peer review) is the author/funder, who has granted bioRxiv a license to display the preprint in perpetuity. It is made available under aCC-BY 4.0 International license.

LEVITT, E. S., ABDALA, A. P., PATON, J. F., BISSONNETTE, J. M. & WILLIAMS, J. T. 2015. μ opioid receptor activation hyperpolarizes respiratory-controlling Kölliker-Fuse neurons and suppresses post-inspiratory drive. J Physiol, 593, 4453-69.

LIANG, X., YONG, Z. & SU, R. 2018. Inhibition of protein kinase A and GIRK channel reverses fentanyl-induced respiratory depression. Neurosci Lett, 677, 14-18.

LORIER, A. R., FUNK, G. D. & GREER, J. J. 2010. Opiate-induced suppression of rat hypoglossal motoneuron activity and its reversal by ampakine therapy. PLoS One, 5, e8766.

LÖTSCH, J., SKARKE, C., SCHNEIDER, A., HUMMEL, T. & GEISSLINGER, G. 2005. The 5-hydroxytryptamine 4 receptor agonist mosapride does not antagonize morphine-induced respiratory depression. Clin Pharmacol Ther, 78, 278-87.

MANZKE, T., GUENTHER, U., PONIMASKIN, E. G., HALLER, M., DUTSCHMANN, M., SCHWARZACHER, S. & RICHTER, D. W. 2003. 5-HT4(a) receptors avert opioid-induced breathing depression without loss of analgesia. Science, 301, 226-9.

MELLEN, N. M., JANCZEWSKI, W. A., BOCCHIARO, C. M. & FELDMAN, J. L. 2003. Opioid-induced quantal slowing reveals dual networks for respiratory rhythm generation. Neuron, 37, 821-6.

MOGRI, M., DESAI, H., WEBSTER, L., GRANT, B. J. & MADOR, M. J. 2009. Hypoxemia in patients on chronic opiate therapy with and without sleep apnea. Sleep Breath, 13, 49-57.

MOLKOV, Y. I., BACAK, B. J., DICK, T. E. & RYBAK, I. A. 2013. Control of breathing by interacting pontine and pulmonary feedback loops. Front Neural Circuits, 7, 16.

MONTANDON, G., QIN, W., LIU, H., REN, J., GREER, J. J. & HORNER, R. L. 2011. PreBotzinger complex neurokinin-1 receptor-expressing neurons mediate opioid-induced respiratory depression. J Neurosci, 31, 1292-301.

MONTANDON, G., REN, J., VICTORIA, N. C., LIU, H., WICKMAN, K., GREER, J. J. & HORNER, R. L. 2016. G-protein-gated Inwardly Rectifying Potassium Channels Modulate Respiratory Depression by Opioids. Anesthesiology, 124, 641-50.

MONTANDON, G. & SLUTSKY, A. S. 2019. Solving the Opioid Crisis: Respiratory Depression by Opioids as Critical End Point. Chest, 156, 653-658.

MOSCA, E. V., CIECHANSKI, P., ROY, A., SCHEIBLI, E. C., BALLANYI, K. & WILSON, R. J. 2014. Methylxanthine reversal of opioid-induced respiratory depression in the neonatal rat: mechanism and location of action. Respir Physiol Neurobiol, 200, 80-9.

MUSTAPIC, S., RADOCAJ, T., SANCHEZ, A., DOGAS, Z., STUCKE, A. G., HOPP, F. A., STUTH, E. A. & ZUPERKU, E. J. 2010. Clinically relevant infusion rates of mu-opioid agonist remifentanil cause bradypnea in decerebrate dogs but not via direct effects in the pre-Bötzinger complex region. J Neurophysiol, 103, 409-18.

OERTEL, B. G., FELDEN, L., TRAN, P. V., BRADSHAW, M. H., ANGST, M. S., SCHMIDT, H., JOHNSON, S., GREER, J. J., GEISSLINGER, G., VARNEY, M. A. & LÖTSCH, J. 2010. Selective antagonism of opioid-induced ventilatory depression by an ampakine molecule in humans without loss of opioid analgesia. Clin Pharmacol Ther, 87, 204-11.

bioRxiv preprint doi: https://doi.org/10.1101/2021.02.24.432816; this version posted February 25, 2021. The copyright holder for this preprint (which was not certified by peer review) is the author/funder, who has granted bioRxiv a license to display the preprint in perpetuity. It is made available under aCC-BY 4.0 International license.

OERTEL, B. G., SCHNEIDER, A., ROHRBACHER, M., SCHMIDT, H., TEGEDER, I., GEISSLINGER, G. & LÖTSCH, J. 2007. The partial 5-hydroxytryptamine1A receptor agonist buspirone does not antagonize morphine-induced respiratory depression in humans. Clin Pharmacol Ther, 81, 59-68.

OVERDYK, F., DAHAN, A., ROOZEKRANS, M., VAN DER SCHRIER, R., AARTS, L. & NIESTERS, M. 2014. Opioid-induced respiratory depression in the acute care setting: a compendium of case reports. Pain Manag, 4, 317-25.

PARK, C. & RUBIN, J. E. 2013. Cooperation of intrinsic bursting and calcium oscillations underlying activity patterns of model pre-Bötzinger complex neurons. J Comput Neurosci, 34, 345-66.

PERSSON, J., SCHEININ, H., HELLSTRÖM, G., BJÖRKMAN, S., GÖTHARSON, E. & GUSTAFSSON, L. L. 1999. Ketamine antagonises alfentanil-induced hypoventilation in healthy male volunteers. Acta Anaesthesiol Scand, 43, 744-52.

PRKIC, I., MUSTAPIC, S., RADOCAJ, T., STUCKE, A. G., STUTH, E. A., HOPP, F. A., DEAN, C. & ZUPERKU, E. J. 2012. Pontine μ-opioid receptors mediate bradypnea caused by intravenous remifentanil infusions at clinically relevant concentrations in dogs. J Neurophysiol, 108, 2430-41.

RAMIREZ, J. M. & BAERTSCH, N. 2018a. Defining the Rhythmogenic Elements of Mammalian Breathing. Physiology (Bethesda), 33, 302-316.

RAMIREZ, J. M. & BAERTSCH, N. A. 2018b. The Dynamic Basis of Respiratory Rhythm Generation: One Breath at a Time. Annu Rev Neurosci, 41, 475-499.

RAMIREZ, J. M., SCHWARZACHER, S. W., PIERREFICHE, O., OLIVERA, B. M. & RICHTER, D. W. 1998. Selective lesioning of the cat pre-Bötzinger complex in vivo eliminates breathing but not gasping. J Physiol, 507 (Pt 3), 895-907.

REN, J., DING, X., FUNK, G. D. & GREER, J. J. 2009. Ampakine CX717 protects against fentanyl-induced respiratory depression and lethal apnea in rats. Anesthesiology, 110, 1364-70.

REN, J., DING, X. & GREER, J. J. 2015. Ampakines enhance weak endogenous respiratory drive and alleviate apnea in perinatal rats. Am J Respir Crit Care Med, 191, 704-10.

REN, J., DING, X. & GREER, J. J. 2019. Activating α4β2 Nicotinic Acetylcholine Receptors Alleviates Fentanyl-induced Respiratory Depression in Rats. Anesthesiology, 130, 1017-1031.

ROSE, A. R., CATCHESIDE, P. G., MCEVOY, R. D., PAUL, D., KAPUR, D., PEAK, E., VAKULIN, A. & ANTIC, N. A. 2014. Sleep disordered breathing and chronic respiratory failure in patients with chronic pain on long term opioid therapy. J Clin Sleep Med, 10, 847-52.

RUBIN, J. E., HAYES, J. A., MENDENHALL, J. L. & DEL NEGRO, C. A. 2009. Calcium-activated nonspecific cation current and synaptic depression promote network-dependent burst oscillations. Proc Natl Acad Sci U S A, 106, 2939-44.

SCHMID, C. L., KENNEDY, N. M., ROSS, N. C., LOVELL, K. M., YUE, Z., MORGENWECK, J., CAMERON, M. D., BANNISTER, T. D. & BOHN, L. M. 2017. Bias Factor and Therapeutic Window Correlate to Predict Safer Opioid Analgesics. Cell, 171, 1165-1175.e13.

bioRxiv preprint doi: https://doi.org/10.1101/2021.02.24.432816; this version posted February 25, 2021. The copyright holder for this preprint (which was not certified by peer review) is the author/funder, who has granted bioRxiv a license to display the preprint in perpetuity. It is made available under aCC-BY 4.0 International license.

SEGERS, L. S., NUDING, S. C., VOVK, A., PITTS, T., BAEKEY, D. M., O'CONNOR, R., MORRIS, K. F., LINDSEY, B. G., SHANNON, R. & BOLSER, D. C. 2012. Discharge Identity of Medullary Inspiratory Neurons is Altered during Repetitive Fictive Cough. Front Physiol, 3, 223.

SMART, J. A., PALLETT, E. J. & DUTHIE, D. J. 2000. Breath interval as a measure of dynamic opioid effect. Br J Anaesth, 84, 735-8.

SMITH, J. C., ABDALA, A. P., BORGMANN, A., RYBAK, I. A. & PATON, J. F. 2013. Brainstem respiratory networks: building blocks and microcircuits. Trends Neurosci, 36, 152-62.

SMITH, J. C., ELLENBERGER, H. H., BALLANYI, K., RICHTER, D. W. & FELDMAN, J. L. 1991a. Pre-Botzinger complex: a brainstem region that may generate respiratory rhythm in mammals. Science, 254, 726-9.

SMITH, J. C., ELLENBERGER, H. H., BALLANYI, K., RICHTER, D. W. & FELDMAN, J. L. 1991b. Pre-Bötzinger complex: a brainstem region that may generate respiratory rhythm in mammals. Science, 254, 726-9.

SORA, I., TAKAHASHI, N., FUNADA, M., UJIKE, H., REVAY, R. S., DONOVAN, D. M., MINER, L. L. & UHL, G. R. 1997. Opiate receptor knockout mice define mu receptor roles in endogenous nociceptive responses and morphine-induced analgesia. Proc Natl Acad Sci U S A, 94, 1544-9.

SUN, X., THÖRN PÉREZ, C., HALEMANI, D. N., SHAO, X. M., GREENWOOD, M., HEATH, S., FELDMAN, J. L. & KAM, K. 2019. Opioids modulate an emergent rhythmogenic process to depress breathing. Elife, 8.

SZÉLL, A., MARTÍNEZ-BELLVER, S., HEGEDÜS, P. & HANGYA, B. 2020. OPETH: Open Source Solution for Real-Time Peri-Event Time Histogram Based on Open Ephys. Front Neuroinform, 14, 21.

TAN, W., JANCZEWSKI, W. A., YANG, P., SHAO, X. M., CALLAWAY, E. M. & FELDMAN, J. L. 2008. Silencing preBötzinger complex somatostatin-expressing neurons induces persistent apnea in awake rat. Nat Neurosci, 11, 538-40.

VAN DER SCHIER, R., ROOZEKRANS, M., VAN VELZEN, M., DAHAN, A. & NIESTERS, M. 2014. Opioid-induced respiratory depression: reversal by non-opioid drugs. F1000Prime Rep, 6, 79.

VAN DORP, E., YASSEN, A., SARTON, E., ROMBERG, R., OLOFSEN, E., TEPPEMA, L., DANHOF, M. & DAHAN, A. 2006. Naloxone reversal of buprenorphine-induced respiratory depression. Anesthesiology, 105, 51-7.

VARGA, A. G., REID, B. T., KIEFFER, B. L. & LEVITT, E. S. 2020. Differential impact of two critical respiratory centres in opioid-induced respiratory depression in awake mice. J Physiol, 598, 189-205.

WALKER, J. M., FARNEY, R. J., RHONDEAU, S. M., BOYLE, K. M., VALENTINE, K., CLOWARD, T. V. & SHILLING, K. C. 2007. Chronic opioid use is a risk factor for the development of central sleep apnea and ataxic breathing. J Clin Sleep Med, 3, 455-61.

bioRxiv preprint doi: https://doi.org/10.1101/2021.02.24.432816; this version posted February 25, 2021. The copyright holder for this preprint (which was not certified by peer review) is the author/funder, who has granted bioRxiv a license to display the preprint in perpetuity. It is made available under aCC-BY 4.0 International license.

WEI, A. D. & RAMIREZ, J. M. 2019. Pre-synaptic Mechanisms and KCNQ Potassium Channels Modulate Opioid Depression of Respiratory Drive. Front Physiol, 10, 1407.

WINTER, S. M., FRESEMANN, J., SCHNELL, C., OKU, Y., HIRRLINGER, J. & HULSMANN, S. 2009. Glycinergic interneurons are functionally integrated into the inspiratory network of mouse medullary slices. Pflugers Arch, 458, 459-69.

WU, J. G., WANG, D., ROWSELL, L., WONG, K. K., YEE, B. J., NGUYEN, C. D., HAN, F., HILMISSON, H., THOMAS, R. J. & GRUNSTEIN, R. R. 2020. The effect of acute exposure to morphine on breathing variability and cardiopulmonary coupling in men with obstructive sleep apnea: A randomized controlled trial. J Sleep Res, 29, e12930.

YANG, C. F. & FELDMAN, J. L. 2018. Efferent projections of excitatory and inhibitory preBötzinger Complex neurons. J Comp Neurol, 526, 1389-1402.

YANG, C. F., KIM, E. J., CALLAWAY, E. M. & FELDMAN, J. L. 2020. Monosynaptic Projections to Excitatory and Inhibitory preBötzinger Complex Neurons. Front Neuroanat, 14, 58.

ZUPERKU, E. J., STUCKE, A. G., HOPP, F. A. & STUTH, E. A. 2017. Characteristics of breathing rate control mediated by a subregion within the pontine parabrachial complex. J Neurophysiol, 117, 1030-1042.

ZUPERKU, E. J., STUCKE, A. G., KROLIKOWSKI, J. G., TOMLINSON, J., HOPP, F. A. & STUTH, E. A. 2019. Inputs to medullary respiratory neurons from a pontine subregion that controls breathing frequency. Respir Physiol Neurobiol, 265, 127-140.

bioRxiv preprint doi: https://doi.org/10.1101/2021.02.24.432816; this version posted February 25, 2021. The copyright holder for this preprint (which was not certified by peer review) is the author/funder, who has granted bioRxiv a license to display the preprint in perpetuity. It is made available under aCC-BY 4.0 International license.

Methods

Animals. Experiments were performed on neonatal (p4-p12) and adult (>p40) male and female C57Bl/6 mice bred at Seattle Children's Research Institute. Homozygous *Oprm1*^{CreGFP} mice were provided by the laboratory of Dr. Richard Palmiter (University of Washington) (Jax Stock No: 035574). *Oprm1*^{CreGFP} were genotyped using a standard protocol with the following three primers: 5' CCT TCC ACT CAG AGA GTG GCG (*Oprm1* forward), 5' CCT TCC ACT CAG AGA GTG GCG (*Oprm1* reverse), and 5' GGC AAA TTT TGG TGT ACG GTC AG (*Cre* reverse). The wild-type allele gives a band of ~500 bp, while the targeted allele gives a band of ~400 bp after 34 cycles with 20-s annealing at 60 °C. *Oprm1*^{CreGFP} mice were crossed with homozygous mice derived at the Allen Brain Institute containing either (1) floxed STOP channelrhodopsin2 fused to EYFP, *Rosa26*$^{lsl\text{-}ChR2:EYFP}$, or more simply *Rosa26*^{ChR2} (Ai32, Jax Stock No: 024109); or (2) floxed STOP ArcherhodopsinT fused to EYFP, *Rosa26*$^{lsl\text{-}ArchT:EYFP}$, or more simply *Rosa26*^{ArchT} (Ai40D, Jax Stock 021188). All mice were group housed with access to food and water *ad libitum* in a temperature controlled (22±1°C) facility with a 12-hr light/dark cycle.

***In vitro* medullary horizontal slice preparation.** Horizontal medullary slices containing the ventral respiratory column were prepared from postnatal day 4-12 mice as previously described (Baertsch et al., 2019). Briefly, whole brainstems were dissected in ice cold, artificial cerebrospinal fluid (aCSF; in mM: 118 NaCl, 3.0 KCl, 25 $NaHCO_3$, 1 NaH_2PO_4, 1.0 $MgCl_2$, 1.5 $CaCl_2$, 30 D-glucose) equilibrated with carbogen (95% O_2, 5% CO_2). aCSF had an osmolarity of 305–312 mOSM and a pH of 7.40– 7.45 when equilibrated with gas mixtures containing 5% CO_2 at ambient pressure. Cyanoacrylate was used to secure the dorsal surface of the brainstem to an agar block cut at a ~15° angle, and a vibratome was used (Leica 1000S) to section the brainstem in the transverse plane in 200-µm steps moving from rostral to caudal until the VII nerves were visualized. Brainstems were then sectioned in the horizontal plane by reorienting the agar block to position its ventral surface facing up. The blade was leveled with the ventral edge of the brainstem and a single ~850-µm step was taken. The angle of the horizontal section through the tissue is determined by the angle at which the agar block was cut and is critical for cutting a horizontal

bioRxiv preprint doi: https://doi.org/10.1101/2021.02.24.432816; this version posted February 25, 2021. The copyright holder for this preprint (which was not certified by peer review) is the author/funder, who has granted bioRxiv a license to display the preprint in perpetuity. It is made available under aCC-BY 4.0 International license.

922 slice at the correct thickness. A partially open “teardrop” shaped central canal is indicative of a properly
923 prepared horizontal slice. The preBötC is located lateral to the rostral end of the teardrop and
924 approximately ½ - ¾ of the distance between the midline and the lateral edge of the tissue.

925 Slices were placed in a custom recording chamber containing circulating aCSF (~15 ml/min)
926 warmed to 30°C. The [K+] in the aCSF was then gradually raised from 3 to 8 mM over ~10 min to elevate
927 neuronal excitability. Glass pipette electrodes (<1MΩ tip resistance) filled with aCSF were placed on the
928 surface of the slice to record rhythmic extracellular neuronal population activity. Signals were amplified
929 10,000X, filtered (low pass, 300 Hz; high pass, 5 kHz), rectified, integrated, and digitized (Digidata 1550A,
930 Axon Instruments). The blind patch clamp approach was used to record the activity of single neurons.
931 Recording electrodes were pulled from borosilicate glass (4-8 MΩ tip resistance) using a P-97
932 Flaming/Brown micropipette puller (Sutter Instrument Co., Novato, CA) and filled with intracellular patch
933 electrode solution containing (in mM): 140 potassium gluconate, 1 $CaCl_2$, 10 EGTA, 2 $MgCl_2$, 4 Na_2ATP,
934 and 10 Hepes (pH 7.2). To map the location of recorded neurons, patch pipettes were backfilled with
935 intracellular patch solution containing 2mg/ml Alexa Fluor568 Hyrdrazide (ThermoFisher). Neuronal
936 activity was recorded in current clamp mode in either cell-attached or whole-cell configuration (depending
937 on the specific experiment as noted in the text) using a MultiClamp 700B amplifier (Molecular Devices,
938 Sunnyvale, CA). Extracellular population activity and intracellular signals were acquired with pCLAMP
939 software (Molecular Devices, Sunnyvale, CA). After cell-attached recordings, the neuronal membrane
940 was ruptured to allow the AlexaFluor fluorescent maker to fill the cell body. Following each experiment,
941 the dorsal surfaces of fresh, unfixed slices were imaged (2.5X) using a Leica DM 4000 B epifluorescence
942 microscope equipped with 405, 488, 548 nm laser lines. Images were post-processed using Image-J
943 software (Version 1.48); brightfield and epifluorescent images of Alexa Fluor 568 labelled cell(s) were
944 overlayed to determine the coordinates of the recorded neuron(s) relative to rostral edge of the slice (VII
945 nerve; Y direction) and the midline (X direction) (Figure 1D, E).

bioRxiv preprint doi: https://doi.org/10.1101/2021.02.24.432816; this version posted February 25, 2021. The copyright holder for this preprint (which was not certified by peer review) is the author/funder, who has granted bioRxiv a license to display the preprint in perpetuity. It is made available under aCC-BY 4.0 International license.

***In vivo* surgical preparation.** Adult mice were induced with isoflurane (~3%) and then transferred to urethane anesthesia (1.5 g/kg, *i.p.*). Mice were then placed supine on a custom heated surgical table to maintain body temp at ~37˚C. The trachea was exposed through a midline incision and cannulated with a curved (180 degree) tracheal tube (24 G) caudal to the larynx and then mice spontaneously breathed 100% O_2 throughout the remainder of the surgery and experimental protocol. ECG leads were placed on the fore and hind paw to monitor heart rate. The trachea and esophagus were removed rostral to the tracheal tube, and the underlying muscles were removed to expose the basal surface of the occipital bone. The portion of the occipital bone and dura overlying the ventral medullary surface were removed, and the exposed surface of the brainstem was superfused with warmed (~37°C) aCSF equilibrated with carbogen (95% O_2, 5% CO_2). The hypoglossal nerve (XII) was isolated unilaterally, cut distally and recorded from using a suction electrode connected to a fire polished pulled glass pipette filled with aCSF. To record multi-unit neuronal population activity directly from the preBötC, tapered pulled glass pipettes with a sharp broken tip (<1MΩ tip resistance) filled with aCSF were advanced into the ventral medulla ~200-500µm until integrated rhythmic activity was maximal. Electrical activity from the brainstem and XII nerve was amplified (10,000X), filtered (low pass 300Hz, high pass 5kHz), rectified, integrated, and digitized (Digidata 1550A, Axon Instruments). In some experiments, extracellular activity was recorded from single units *in vivo* using 4-8 MΩ pulled glass electrodes filled with aCSF. Prior to experimental protocols, adequate depth of anesthesia was determined via heart rate and respiratory responses to toe pinch and adjusted if necessary with supplemental urethane (*i.p.*).

Optogenetic and pharmacological manipulations. 200-µm diameter glass fiber optics (0.24NA) connected to blue (470 nm) high-powered LEDs or yellow-orange (598 nm) lasers were positioned above the preBötC either bilalaterally, or ipsilateral/contralateral to the population and/or unit recordings depending on the specific experiment (as indicated in the text and figure legends). Light power was calibrated using an optical power meter (ThorLabs). Powers and durations of light pulses are noted in the text and figures. During single unit recordings *in vitro* using the blind patch approach, neurons were

bioRxiv preprint doi: https://doi.org/10.1101/2021.02.24.432816; this version posted February 25, 2021. The copyright holder for this preprint (which was not certified by peer review) is the author/funder, who has granted bioRxiv a license to display the preprint in perpetuity. It is made available under aCC-BY 4.0 International license.

971 classified as *Oprm1*+ based on optogenetic responses. In *Oprm1*^{CreGFP}; *Rosa26*$^{ArchT:EYFP}$ slices, neurons
972 that were inhibited during 598nm light were designated as *Oprm1*+, whereas those that lacked a
973 response were presumed to be *Oprm1*-. In *Oprm1*$^{Cre:GFP}$; *Rosa26*$^{ChR2:EYFP}$ slices, Oprm1 expression was
974 determined using one or both of the following methods: (1) the presence of an excitatory response to
975 light following pharmacological blockade of glutamatergic synaptic transmission (20 µM CNQX, 20 µM
976 CPP); (2) the presence of spikes generated reliably and with short latency ~5-10 ms following brief 10ms
977 470 nm light pulses ipsilateral to the recording electrode (e.g. see Figure 5A-C). In many cases these
978 strategies were used in combination to characterize neurons as *Oprm1*+ or *Oprm1*-.

979 During *in vitro* experiments, stable baseline preBötC population and single-unit activities were
980 recorded for ≥5min prior to addition of the MOR-agonist DAMGO ([D-Ala2, N-Me-Phe4, Gly5-ol]-
981 Enkephalin) to the circulating aCSF bath. DAMGO (Sigma Aldrich) stock solutions (1 mM in H_2O) were
982 aliquoted, and stored at -20˚C. In dose-response experiments, DAMGO was added to the aCSF bath at
983 total concentrations of 50, 100, 200, and 300 nM at 7-min intervals, and data were analyzed during the
984 last 2 min of each interval. In some experiments, MOR activation was reversed with the competitive MOR
985 antagonist Naloxone (Nx) and AMPAR- and NMDAR-dependent glutamatergic synaptic transmission
986 was blocked by adding CNQX (6-Cyano-7-nitroquinoxaline-2,3-dione disodium) and (R)-CPP (3-((R)-2-
987 Carboxypiperazin-4-yl)-propyl-1-phosphonic acid) to the aCSF bath. Naloxone (Tocris) was diluted to a
988 100 mM stock solution in H_2O. CNQX and CPP (Tocris) were diluted to 20 mM stock solutions in H_2O.
989 All drugs were aliquoted and stored at -20˚C. For experiments *in vivo,* stable baseline preBötC and XII
990 multi-unit activity was established for ≥5 min prior to systemic injection of morphine (150 mg/kg; Patterson
991 Veterinary Supply).

992 **Constructing a computational model of OIRD in the preBötC.** The computational model of the
993 preBötC consisted of 300 Hodgkin-Huxley style neurons with equations modified from (Butera et al.,
994 1999a, Butera et al., 1999b). The membrane voltage of each neuron is given by:

bioRxiv preprint doi: https://doi.org/10.1101/2021.02.24.432816; this version posted February 25, 2021. The copyright holder for this preprint (which was not certified by peer review) is the author/funder, who has granted bioRxiv a license to display the preprint in perpetuity. It is made available under aCC-BY 4.0 International license.

$$C_m \frac{dv}{dt} = I_{Na} + I_K + I_{leak} + I_{NaP} + I_{opioid} + I_{syn}$$

Where the currents are

$$I_{Na} = g_{Na} \cdot m_\infty^3 \cdot (1 - n) \cdot (v - E_{Na})$$

$$I_K = g_K \cdot n^4 \cdot (v - E_K)$$

$$I_{NaP} = g_{NaP} \cdot m_{NaP_\infty} \cdot h \cdot (v - E_{Na})$$

$$I_{leak} = g_{leak} \cdot (v - E_{leak})$$

$$I_{opioid} = \begin{cases} I_{opioid}, & Oprm1^+ \\ 0pA, & Oprm1^- \end{cases}$$

And:

$$\frac{dn}{dt} = \frac{(n_\infty - n)}{\tau_n}$$

$$\frac{dh}{dt} = \frac{(h_\infty - h)}{\tau_h}$$

$$m_\infty = \frac{1}{1 + e^{\left(\frac{v - v_m}{\sigma_m}\right)}}$$

$$n_\infty = \frac{1}{1 + e^{\left(\frac{v - v_n}{\sigma_n}\right)}}$$

$$m_{NaP_\infty} = \frac{1}{1 + e^{\left(\frac{v - v_{m_{NaP}}}{\sigma_{m_{NaP}}}\right)}}$$

$$h_\infty = \frac{1}{1 + e^{\left(\frac{v - v_h}{\sigma_h}\right)}}$$

$$\tau_n = \frac{\tau_{nb}}{cosh\left(\frac{v - v_n}{2\sigma_n}\right)}$$

$$\tau_h = \frac{\tau_{hb}}{cosh\left(\frac{v - v_h}{2\sigma_h}\right)}$$

The synaptic currents for neuron post-synaptic neuron *i* are given by (REF Destexhe):

bioRxiv preprint doi: https://doi.org/10.1101/2021.02.24.432816; this version posted February 25, 2021. The copyright holder for this preprint (which was not certified by peer review) is the author/funder, who has granted bioRxiv a license to display the preprint in perpetuity. It is made available under aCC-BY 4.0 International license.

$$I_{syn,i} = \sum_{j \in OPRM1^{+}: j \to i} (1 - syn_{opioid}) \cdot g_E s_{ij} \left(V_i - E_{synE}\right)$$

$$+ \sum_{j \in OPRM1^{-}: j \to i} g_E s_{ij} \left(V_i - E_{synE}\right) + \sum_{j \in I: j \to i} g_I s_{ij} \left(V_i - E_{synI}\right)$$

So that if pre-synaptic neuron *j* is *Oprm1*$^{+}$, the excitatory conductance of the $j \to i$ synapse is scaled by the controlled parameter $syn_{opioid} = [0,1]$. The dynamics of the synapses are governed by:

$$\frac{ds}{dt} = \frac{\left(1 - s_{ij}\right) m_{\infty}^{(ij)}\left(V_j\right) - s_{ij}}{\tau_{syn}}$$

$$m_{\infty}^{(ij)}\left(V_j\right) = \frac{1}{1 + e^{\frac{V_j - \theta_{syn}}{\sigma_{syn}}}}$$

Global parameters are listed in Table 1, and cell specific parameters are listed in Table 2.

We vary I_{opioid} from 0 to 6 pA in steps of 0.5 pA, and syn_{opioid} from 0 to 0.6 in steps of 0.05. I_{opioid} and syn_{opioid} were set to zero during "control" conditions, and to a proscribed value during simulated MOR activation. Connectivity was generated randomly with probability $p = \frac{k_{avg}}{2(N-1)}$ where $k_{avg} = 6; N = 300$. Eight replicates were performed of each combination of I_{opioid} and syn_{opioid} by initializing the random number generator with an integer seed in [0,7]. All simulations were performed in python using Brian2, and code is available at https://github.com/nbush257/oprm1 and upon request.

Simulated population rates were smoothed with a gaussian kernel with $\sigma = 25\ ms$, and bursts were defined as excursions of the population rate above 10 sp/s.

Quantification and statistical analysis. *Effects of MOR activation on the spiking activity of individual preBötC neurons* (Figure 2), were quantified from ~10-20 consecutive respiratory cycles during the last 2min of each dose of DAMGO. Action potentials and integrated preBötC population bursts were detected using the threshold search function in Clampfit (Molecular Devices). Spike times were compared to onset

bioRxiv preprint doi: https://doi.org/10.1101/2021.02.24.432816; this version posted February 25, 2021. The copyright holder for this preprint (which was not certified by peer review) is the author/funder, who has granted bioRxiv a license to display the preprint in perpetuity. It is made available under aCC-BY 4.0 International license.

and offset times of preBötC population bursts to quantify spike frequencies specifically between (inter-burst interval) or during bursts. For pre-inspiratory neurons, average spiking frequency at baseline and in 300nM DAMGO was also quantified over the course of the inter-burst interval. Spike times were normalized relative to the duration of each IBI, and instantaneous spike frequencies were averaged within 1000-time bins between the start and end of the IBI. To quantify changes in total preBötC population spiking *in vitro* and *in vivo* between inspiratory bursts (IBI) in response to MOR activation, background noise was measured with in the aCSF bath, but prior to contacting the surface of slices with the recording electrode. This noise value was then subtracted from the amplitude of the integrated population recording during ~10-20 consecutive IBIs to estimate "total spiking activity" during this period (Figure 3A). IBI spiking was then measured during subsequent MOR activation or optogenetic manipulations and normalized to the baseline value. Failed bursts were distinguished from successful bursts in they were >2 standard deviations from the mean burst amplitude. MOR induced changes in evoked EPSP amplitudes (Figure 5D,E) were determined by unilaterally stimulating *Oprm1*+ preBötC neurons while recording V_m from neurons in the contralateral preBötC. In responsive neurons, 50-100 trials containing a 10ms light pulse were delivered at baseline, and in 50 and 300 nM DAMGO and evoked EPSP amplitudes were averaged across all trials.

Statistical comparisons were performed using GraphPad Prism8 software. Groups were compared using appropriate two-tailed t-tests, or one-way or two-way ANOVAs with Bonferonni's multiple comparisons post hoc tests. Differences were considered significant at $p<0.05$ and data are displayed as means±standard error. For all post hoc statistical comparisons, p-values are designated in the figures as follows: * $p<0.05$, # $p<0.01$, † $p<0.001$, ‡ $p<0.0001$. Data was visualized and figures were assembled using a combination of Clampfit, GraphPad, and PowerPoint software.

bioRxiv preprint doi: https://doi.org/10.1101/2021.02.24.432816; this version posted February 25, 2021. The copyright holder for this preprint (which was not certified by peer review) is the author/funder, who has granted bioRxiv a license to display the preprint in perpetuity. It is made available under aCC-BY 4.0 International license.

Figures and Legends

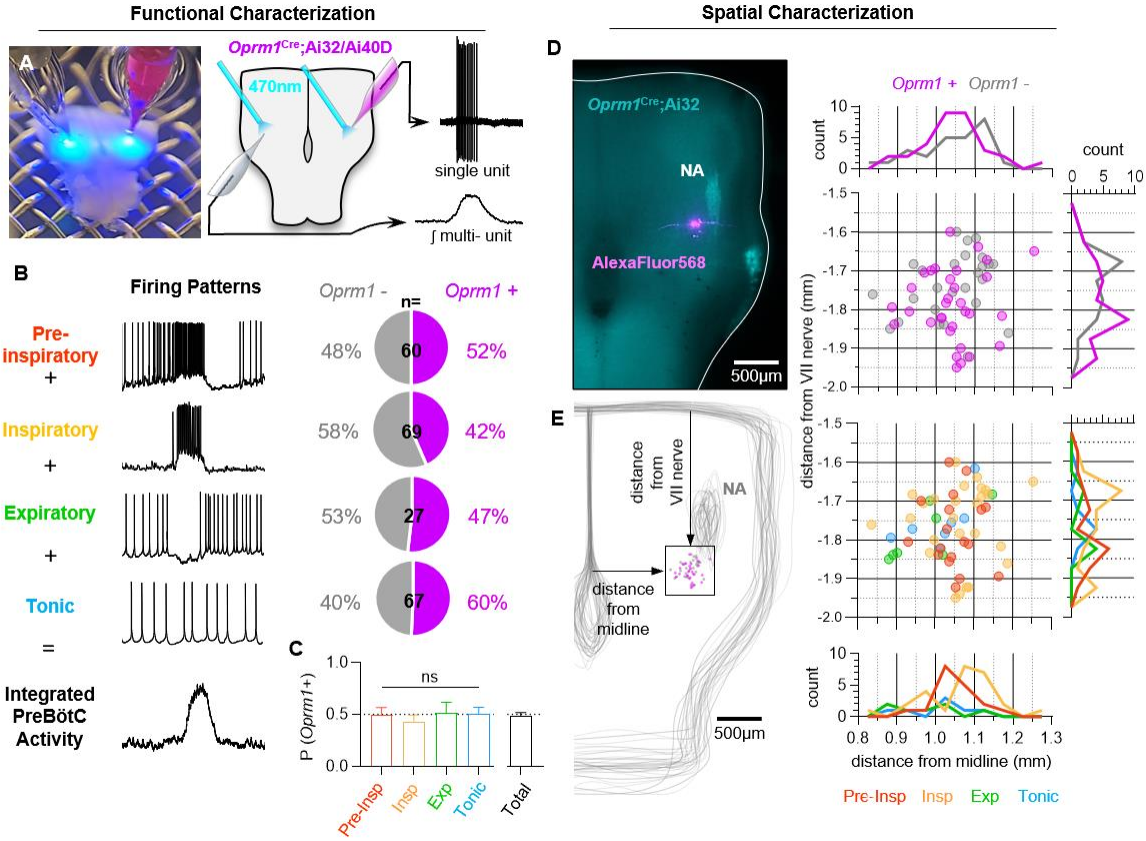

Figure 1: *Characterization of Oprm1+ neuron discharge identities and spatial distributions in the preBötC.* **A**) Image (left) and schematic (right) illustrating the approach to optotag functionally identified single units in horizontal brainstem slices. **B**) Discharge identities of n= 223 preBötC neurons and quantification of *Oprm1* expression among each type demonstrating that **C**) *Oprm1* is evenly expressed in ~50% of all preBötC neuron types [one-way ANOVA (p=0.82) with Bonferroni post hoc tests]. **D**) Image of EYFP (cyan) and Alexa598 (magenta) fluorescence in a *Oprm1*^{Cre}; *Rosa26*^{ChR2} (Ai32) horizontal brainstem slice following an intracellular recording experiment. Note the enriched expression of *Oprm1* within the nucleus ambiguus (NA). **E**) Quantified locations of (n=58) recorded preBötC neurons, caudal and slightly medial to the compact region of the NA, and 2D distributions in the horizontal plane of *Oprm1*+ and *Oprm1*- neurons and pre-inspiratory (pre-Insp), inspiratory (insp), expiratory (exp), and tonic neurons.

bioRxiv preprint doi: https://doi.org/10.1101/2021.02.24.432816; this version posted February 25, 2021. The copyright holder for this preprint (which was not certified by peer review) is the author/funder, who has granted bioRxiv a license to display the preprint in perpetuity. It is made available under aCC-BY 4.0 International license.

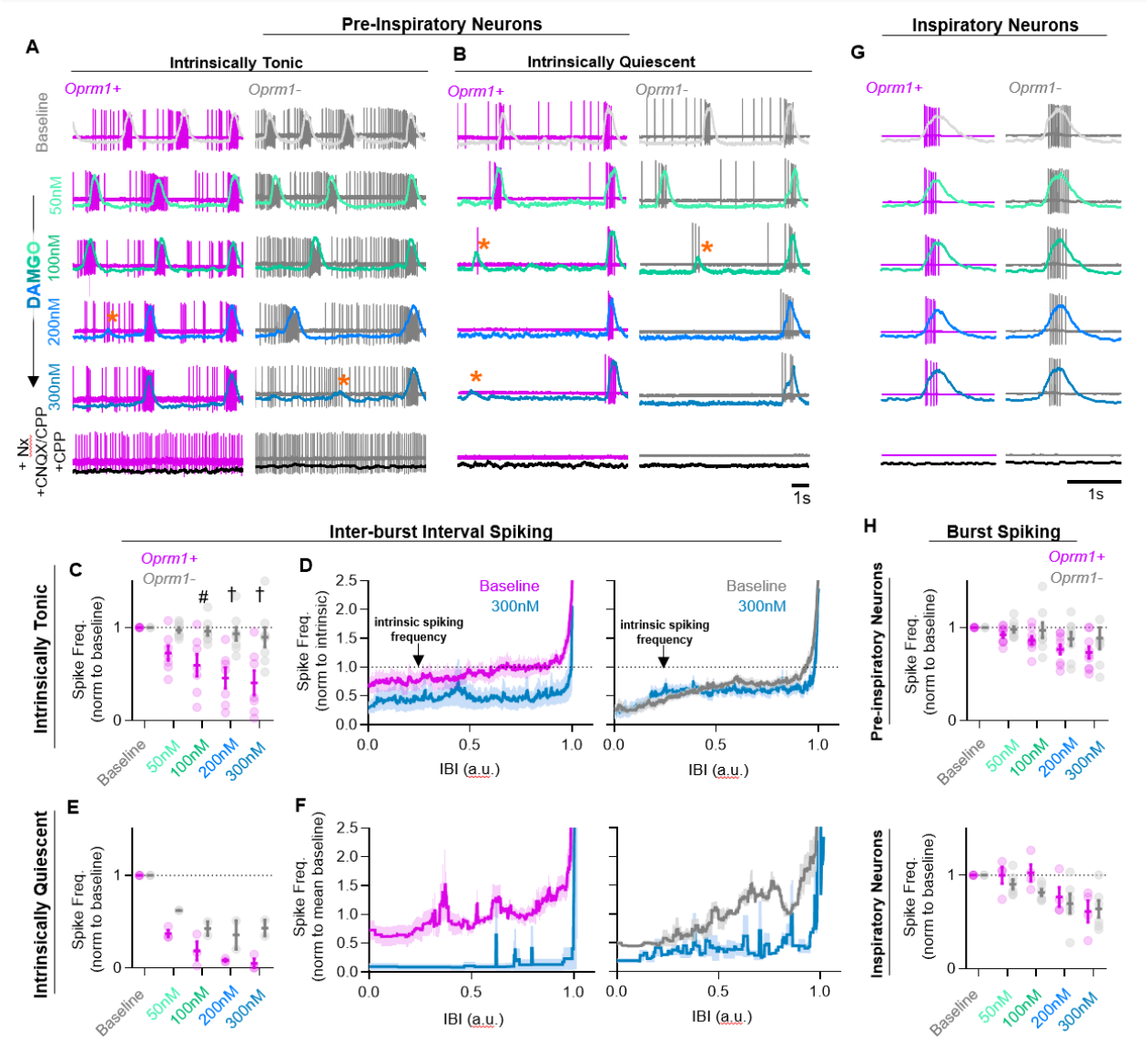

Figure 2: *Effects of MOR activation on spiking activity of pre-inspiratory and inspiratory preBötC neurons.* Example cell-attached recordings from *Oprm1*+ and *Oprm1*- intrinsically tonic (**A**) and intrinsically quiescent (**B**) pre-inspiratory neurons during increasing concentrations of DAMGO (50-300 nM) and following subsequent blockade of MOR activation (5 μM Naloxone, Nx) and excitatory synaptic transmission (20 μM CNQX and CPP). Orange asterisks indicate burst failures. **C**) Comparison of average IBI spiking frequency from intrinsically tonic *Oprm1*+ and *Oprm1*- pre-inspiratory neurons during increasing concentrations of DAMGO [two-way RM ANOVA (p=0.003) and Bonferroni post hoc tests). **D**) Instantaneous spike frequency normalized to intrinsic spiking activity (dotted line) of *Oprm1*+ and *Oprm1*- neurons during the IBI at baseline and in 300 nM DAMGO. **E**) Average IBI spiking frequency from intrinsically quiescent *Oprm1*+ and *Oprm1*- pre-inspiratory neurons during increasing concentrations of DAMGO [two-way RM ANOVA (p=0.045) and Bonferroni post hoc tests]. **F**) Instantaneous spike frequency normalized to mean baseline IBI spike rate of *Oprm1*+ and *Oprm1*- neurons during the IBI at baseline and in 300 nM DAMGO. **G**) Example cell-attached recordings from *Oprm1*+ and *Oprm1*- inspiratory neurons during increasing concentrations of DAMGO and following subsequent application of Naloxone and blockade of excitatory synaptic transmission. **H**) Comparison of average spike frequencies during inspiratory bursts (norm to baseline) in *Oprm1*+ and *Oprm1*- pre-inspiratory neurons (top) (two-way RM ANOVA, p=0.187) and inspiratory neurons (bottom) (two-way RM ANOVA, p=0.41) during increasing concentrations of DAMGO.

bioRxiv preprint doi: https://doi.org/10.1101/2021.02.24.432816; this version posted February 25, 2021. The copyright holder for this preprint (which was not certified by peer review) is the author/funder, who has granted bioRxiv a license to display the preprint in perpetuity. It is made available under aCC-BY 4.0 International license.

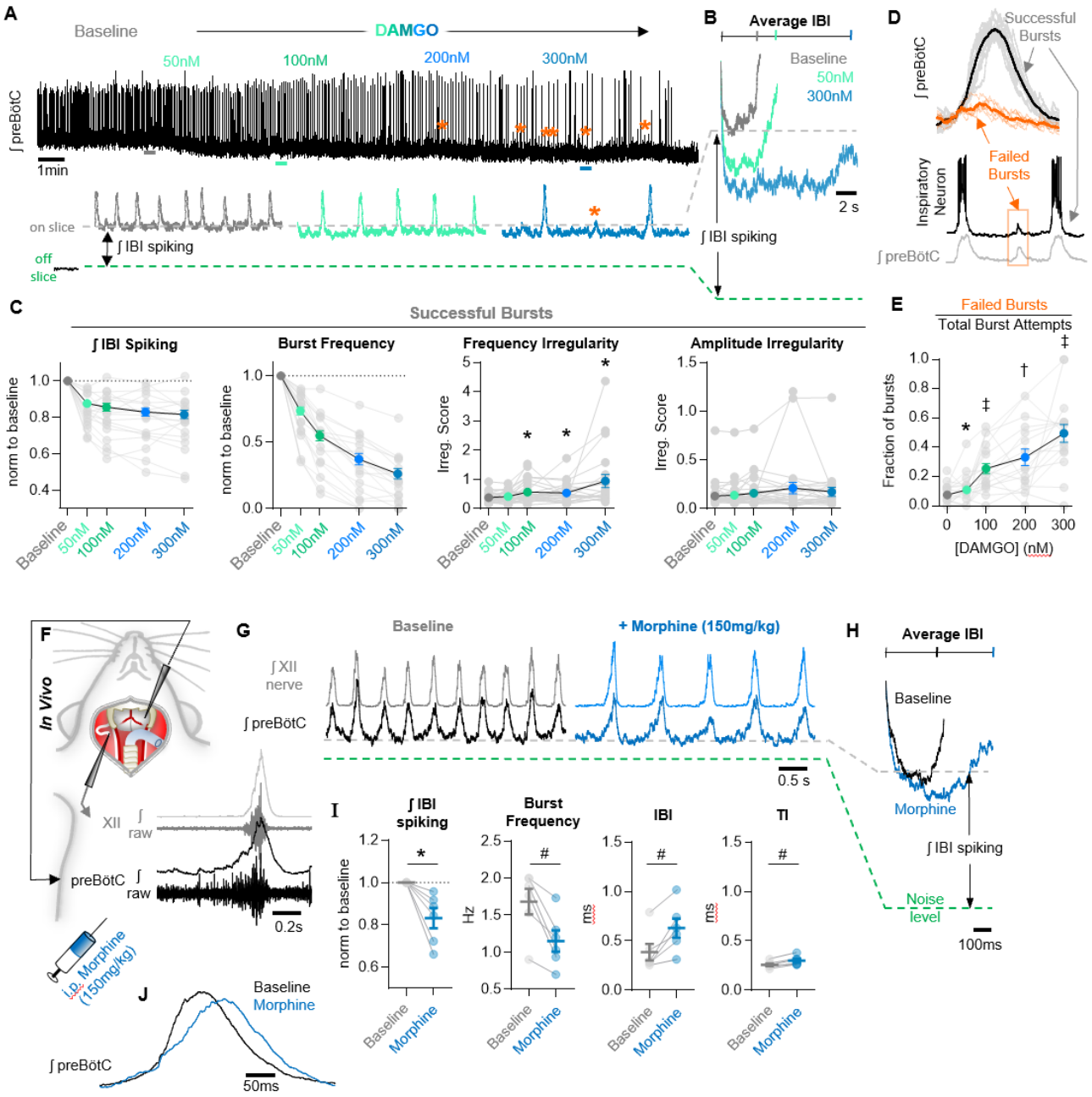

Figure 3: *Network-level effects of MOR activation on spiking activity in the preBötC in vitro and in vivo.* **A**) Representative ∫preBötC activity from a horizontal slice during increasing concentrations of DAMGO. Orange asterisks indicate burst failures. **B**) Averaged inter-burst intervals at baseline and in DAMGO demonstrating changes in IBI spiking. **C**) Quantified IBI spiking, burst frequency, frequency irregularity, and amplitude irregularity (n=30) (one-way ANOVA with Bonferroni post hoc tests). **D**) Averaged successful bursts compared to burst failures (top) and example intracellular recording during a failed burst (bottom). **E**) Quantified fraction of burst failures during increasing concentrations of DAMGO [RM mixed-effects model (p<0.0001) with Bonferroni post hoc tests]. **F**) Schematic of *in vivo* experimental preparation with example simultaneous ∫XII and ∫preBötC recordings. **G**) Representative ∫XII and ∫preBötC activity at baseline and following *i.p.* morphine. **H**) Averaged IBIs at baseline and following morphine. **I**) Quantified IBI spiking, breathing frequency, inter-burst interval, and inspiratory time (TI) (n=6; ratio paired t-tests). **J**) Example changes in preBötC burst morphology in response to morphine administration *in vivo*.

bioRxiv preprint doi: https://doi.org/10.1101/2021.02.24.432816; this version posted February 25, 2021. The copyright holder for this preprint (which was not certified by peer review) is the author/funder, who has granted bioRxiv a license to display the preprint in perpetuity. It is made available under aCC-BY 4.0 International license.

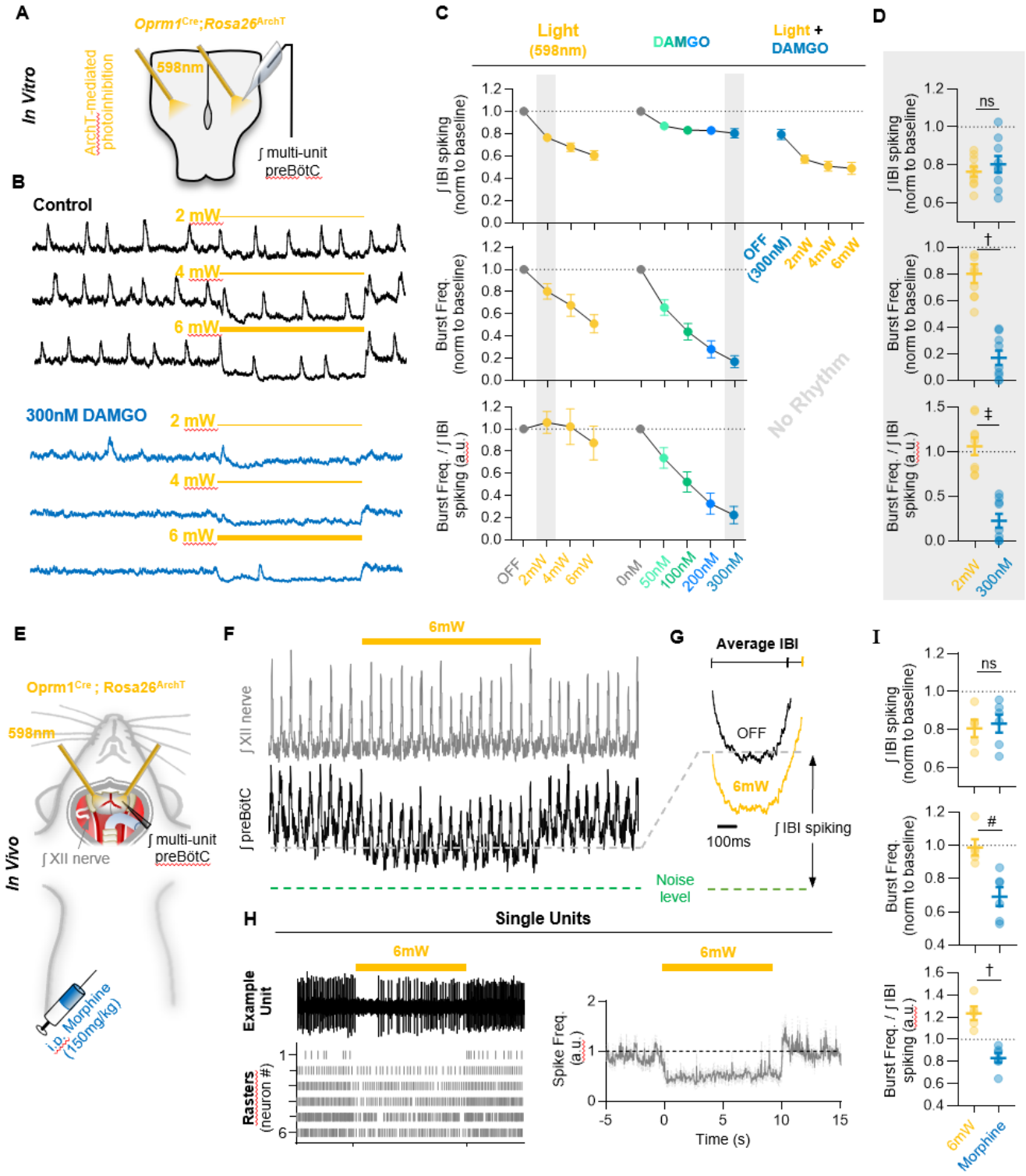

Figure 4: *Mimicking opioid induced changes in preBötC spiking does not phenocopy OIRD.* **A**) Schematic of experimental design using *Oprm1*^{Cre};*Rosa26*^{ArchT} horizontal brainstem slices. **B**) Example ∫preBötC recordings during bilateral photoinhbition of preBötC^{Oprm1} neurons at baseline and following OIRD. Note the continued suppression of preBötC spiking activity following silencing of rhythmogenesis with DAMGO. **C**) Quantification of ∫IBI spiking, burst frequency, and the burst frequency/∫IBI spiking ratio in n=9 slices during

bioRxiv preprint doi: https://doi.org/10.1101/2021.02.24.432816; this version posted February 25, 2021. The copyright holder for this preprint (which was not certified by peer review) is the author/funder, who has granted bioRxiv a license to display the preprint in perpetuity. It is made available under aCC-BY 4.0 International license.

baseline photoinhibition of *Oprm1*+ preBötC neurons, during increasing concentrations of DAMGO, and during photoinhibition in 300 nM DAMGO. **D**) Comparison of changes in IBI spiking, burst frequency, and the burst frequency/IBI spiking ratio during 2mW photoinhibition and 300 nM DAMGO. Data corresponds to gray highlighted regions in panel C. (two-tailed paired t-tests). **E**) Schematic of anesthetized *in vivo* experimental preparation and **F**) example ∫XII and ∫preBötC recordings during bilateral photoinhibition of *Oprm1*+ preBötC neurons. **G**) Average ∫IBI spiking activity at baseline (OFF) and during photoinhibition. **H**) Example single unit recording (top left) rasters (bottom left), and average spike frequency (right) from n=6 preBötC neurons during a 10-s pulse of 598 nm 6 mW light. **I**) Comparison of changes in IBI spiking, burst frequency, and the burst frequency/IBI spiking ratio elicited during 6-mW bilateral photoinhibition and following *i.p.* morphine (two-tailed paired t-tests).

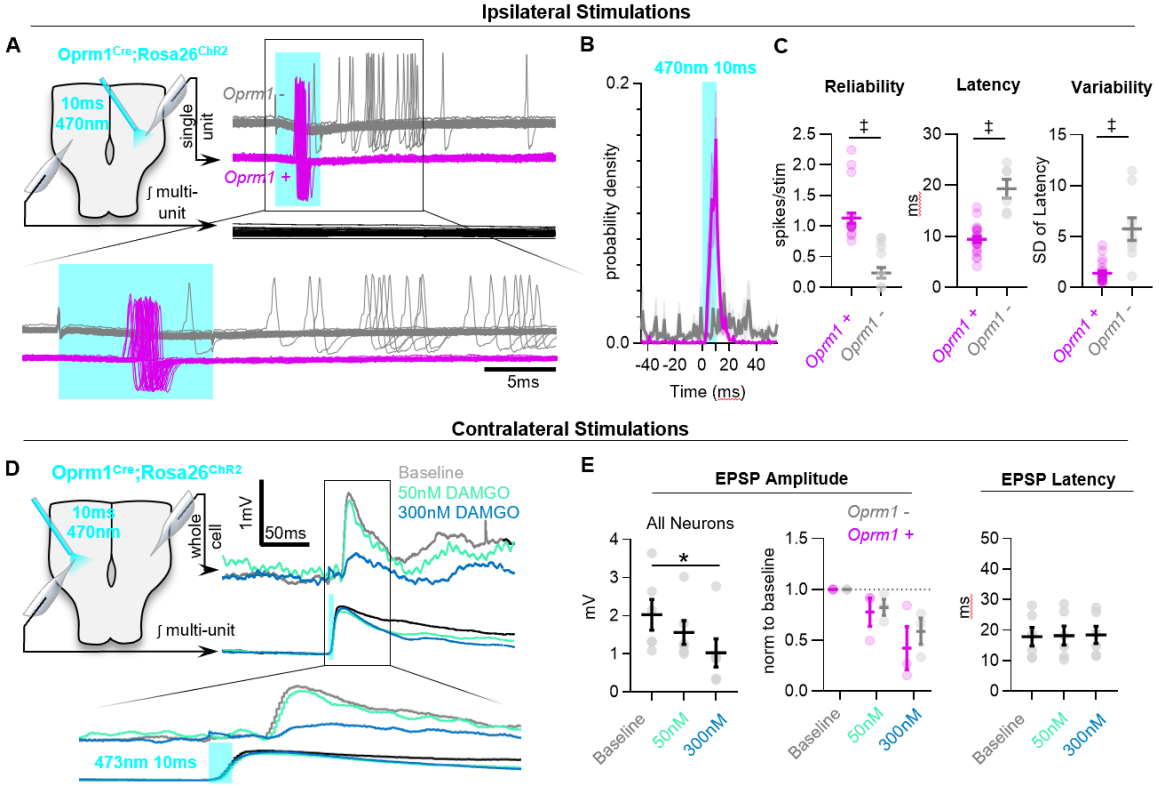

Figure 5: *MOR activation impairs synaptic transmission in the preBötC.* **A**) Example responses of *Oprm1*+ and *Oprm1*- preBötC neurons to direct (ipsilateral) photostimulation. **B**) Probability density histogram of spikes before, during, and after and 10ms light pulse (1ms bins). **C**) Quantified number of spikes evoked per stimulation, latency to spike from light onset, and variability in spike latencies from n=22 *Oprm1*+ and n=6 *Oprm1*- neurons (unpaired t-tests). **D**) Example experiment showing averaged EPSPs evoked during contralateral photostimulation under baseline conditions and in 50 and 300 nM DAMGO (n=6 of 30 neurons exhibited EPSPs during contralateral stimulations). **E**) Quantified evoked EPSP amplitudes and latencies from n=6 neurons [left: RM one-way ANOVA (p=0.011); middle: RM two-way ANOVA (p=0.600); right: RM one-way ANOVA (p=0.511)].

bioRxiv preprint doi: https://doi.org/10.1101/2021.02.24.432816; this version posted February 25, 2021. The copyright holder for this preprint (which was not certified by peer review) is the author/funder, who has granted bioRxiv a license to display the preprint in perpetuity. It is made available under aCC-BY 4.0 International license.

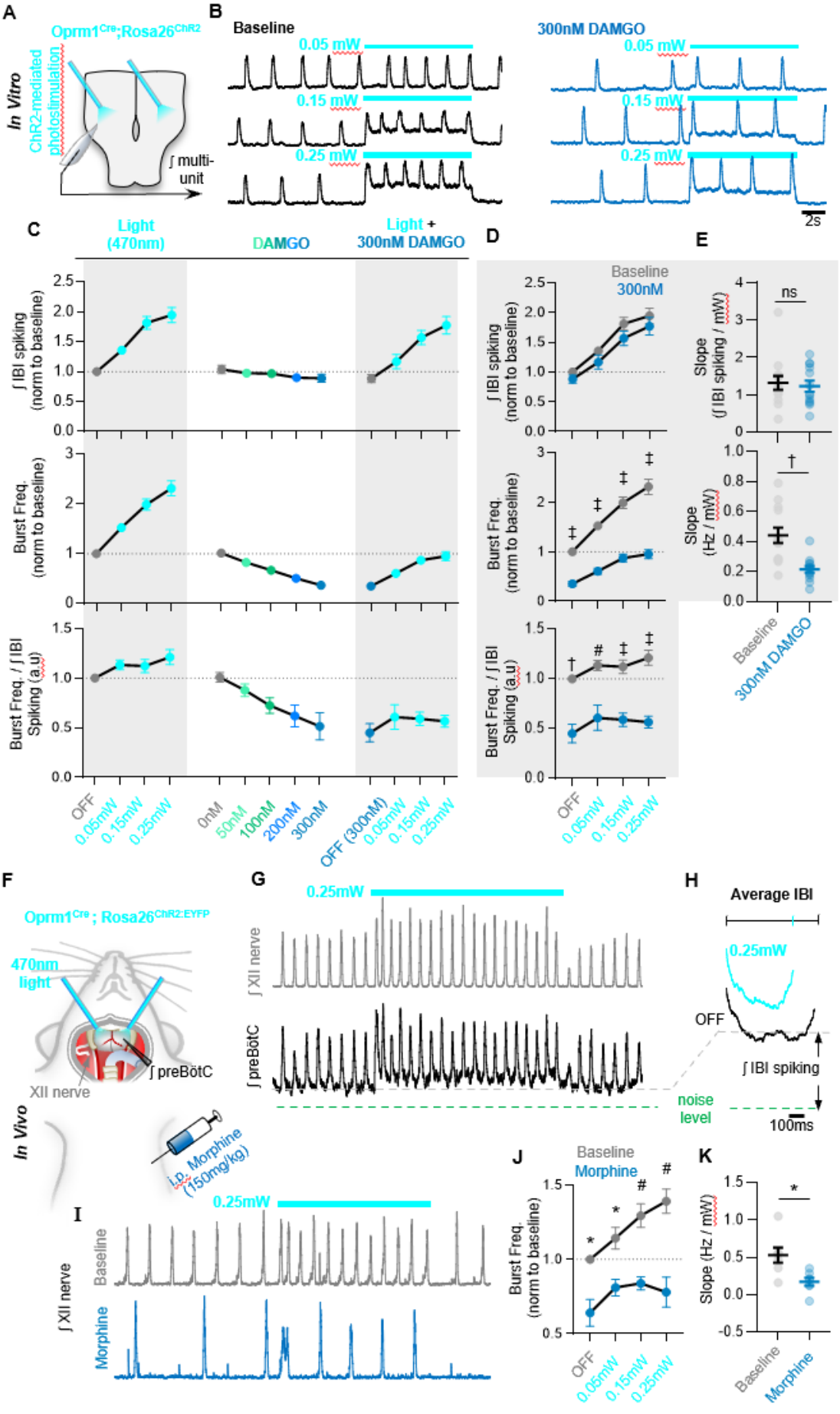

bioRxiv preprint doi: https://doi.org/10.1101/2021.02.24.432816; this version posted February 25, 2021. The copyright holder for this preprint (which was not certified by peer review) is the author/funder, who has granted bioRxiv a license to display the preprint in perpetuity. It is made available under aCC-BY 4.0 International license.

Figure 6: *The ability of Oprm1+ neurons to drive preBötC activity is reduced by MOR activation.* **A**) Experimental schematic and **B**) example preBötC activity at baseline and in 300 nM DAMGO during bilateral photostimulation of *Oprm1*+ neurons. **C**) Quantification of ∫IBI spiking, burst frequency, and the burst frequency/∫IBI spiking ratio in n=13 slices during baseline photostimulation of *Oprm1*+ preBötC neurons, during increasing concentrations of DAMGO, and during photoinhibition in 300 nM DAMGO. **D**) Comparison of light-induced changes in IBI spiking, burst frequency, and the burst frequency/IBI spiking ratio. Data corresponds to gray highlighted regions in panel C (two-way ANOVA). **E**) Quantified slope of IBI spiking and burst frequency responses to increasing power of light stimulations (paired t-tests). **F**) Schematic of in-vivo preparation and **G**) representative ∫XII and ∫preBötC activity during 10-s bilateral photostimulation of *Oprm1*+ neurons. **H**) Averaged ∫IBI activity at baseline (OFF) and during photostimulation. **I**) Example inspiratory rhythm (XII) during bilateral photostimulation at baseline and following *i.p.* morphine. **J**) Quantified changes in inspiratory frequency evoked by photostimulation at baseline and after morphine from n=5 anesthetized mice (two-way ANOVA). **K**) Quantified slope of burst frequency responses to increasing power of light stimulations (paired t-test).

bioRxiv preprint doi: https://doi.org/10.1101/2021.02.24.432816; this version posted February 25, 2021. The copyright holder for this preprint (which was not certified by peer review) is the author/funder, who has granted bioRxiv a license to display the preprint in perpetuity. It is made available under aCC-BY 4.0 International license.

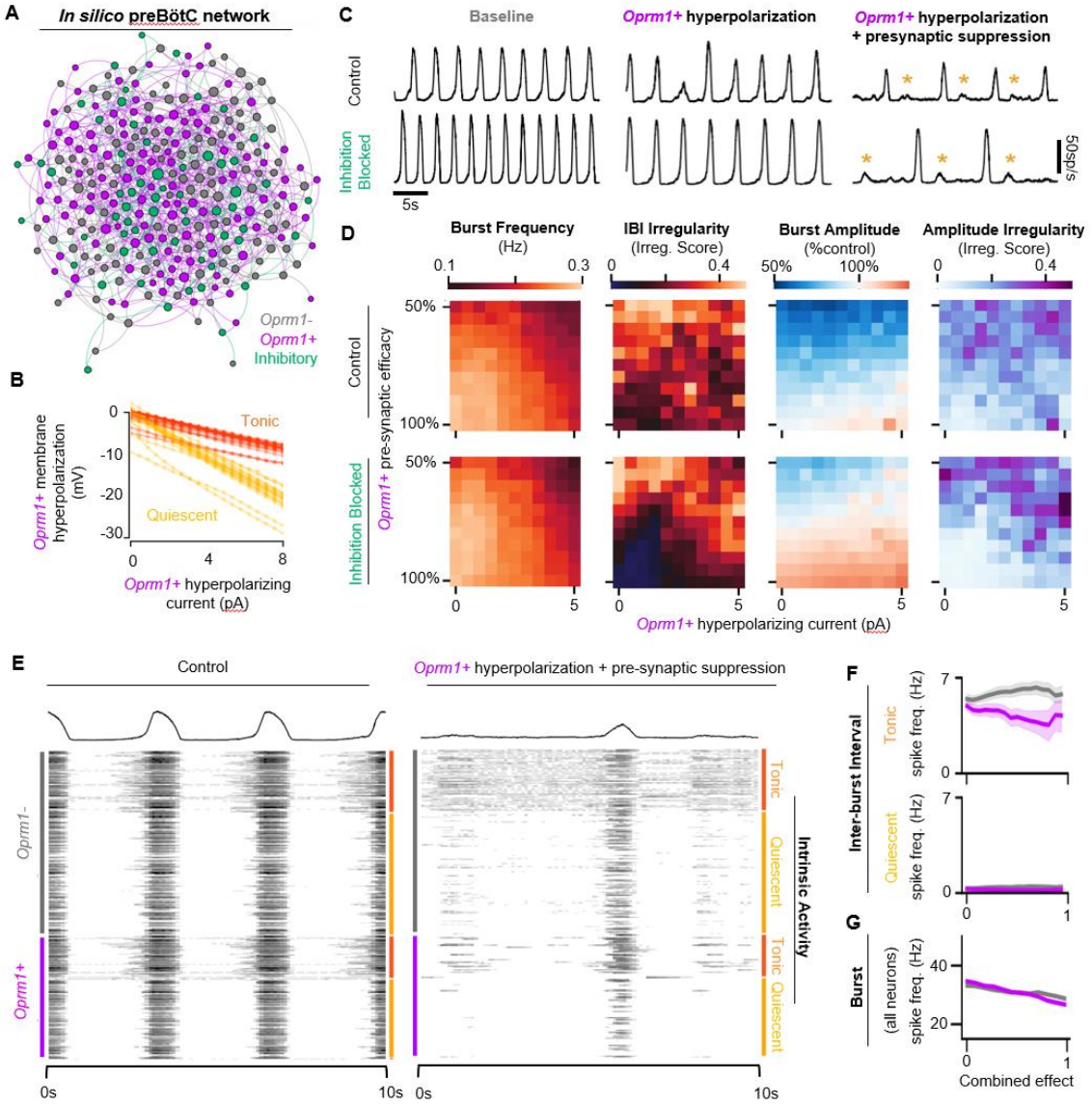

Figure 7: Modelling preBötC MOR activation *in silico.* **A)** Example model network structure. Model networks were connected randomly and contained excitatory (80%) and inhibitory neurons (20%) that were intrinsically tonic (35%) or quiescent (65%). Half of all excitatory neurons were designated as *Oprm1+*. Node size and centrality represent the number of synaptic connections. **B)** Current/Voltage plots for intrinsically tonic (n=17) and quiescent (n=31) *Oprm1+* model neurons for the applied opioid driven hyperpolarization. **C)** Example rhythmic activity from the network shown in (A) at baseline, during 6 pA hyperpolarization of *Oprm1+* neurons, and during 6 pA hyperpolarization and a 45% reduction in pre-synaptic efficacy of *Oprm1+* neurons. Orange asterisks indicate burst failures. **D)** Heat maps showing the isolated and combined effects of *Oprm1+* neuron hyperpolarization and pre-synaptic suppression on characteristics of the network rhythm. **E)** Example spiking activity of all 300 neurons in the model network at baseline and during simulated MOR activation (6pA hyperpolarization and 45% pre-synaptic suppression of *Oprm1+* neurons). **F)** Quantified inter-burst interval (IBI) spike frequencies of intrinsically tonic and quiescent *Oprm1+* and *Oprm1-* neurons during simulated MOR activation. **G)** Spike frequency during network bursts for all *Oprm1+* and *Oprm1-* model neurons during simulated MOR activation (combined effect of 1 designates 6pA hyperpolarization and 55% pre-synaptic efficacy of *Oprm1+* neurons). Data shown as mean±SE.

bioRxiv preprint doi: https://doi.org/10.1101/2021.02.24.432816; this version posted February 25, 2021. The copyright holder for this preprint (which was not certified by peer review) is the author/funder, who has granted bioRxiv a license to display the preprint in perpetuity. It is made available under aCC-BY 4.0 International license.

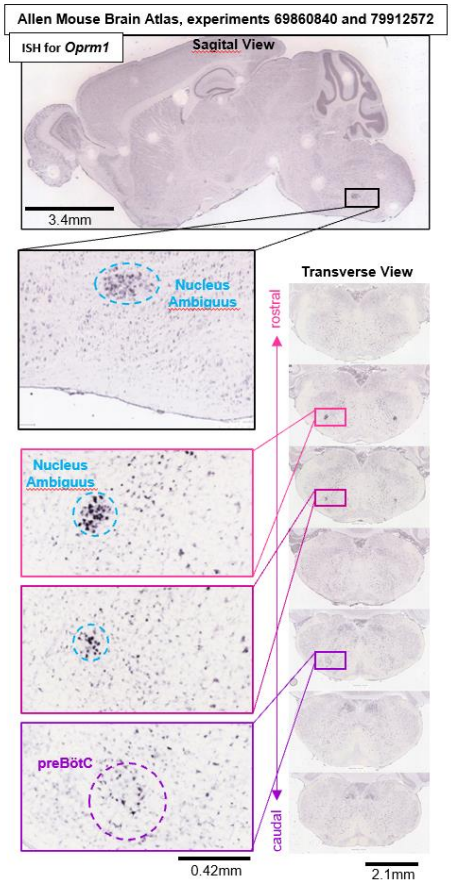

Supplemental Figure 1: *Oprm1* in situ hybridization experiments #69860840 and #79912572 from the Allen Mouse Brain Atlas (Lein et al., 2007) (https://mouse.brain-map.org/search/show?page_num=0&page_size=25&no_paging=false&exact_match=false&search_term=Oprm1&search_type=gene) showing diffuse expression of *Oprm1* gene transcripts within the preBötC region and adjacent Nucleus Ambiguus.

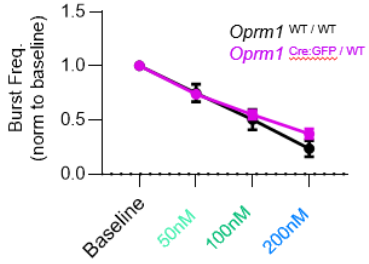

Supplemental Figure 2: DAMGO has similar effects on inspiratory burst frequency generated by wild-type (*Oprm1*$^{WT\ /\ WT}$) and heterozygous (*Oprm1* $^{Cre:GFP\ /\ WT}$) horizontal brainstems slices. Two-way RM ANOVA with Bonferroni's multiple comparisons tests. Data shown and means±SE.

bioRxiv preprint doi: https://doi.org/10.1101/2021.02.24.432816; this version posted February 25, 2021. The copyright holder for this preprint (which was not certified by peer review) is the author/funder, who has granted bioRxiv a license to display the preprint in perpetuity. It is made available under aCC-BY 4.0 International license.

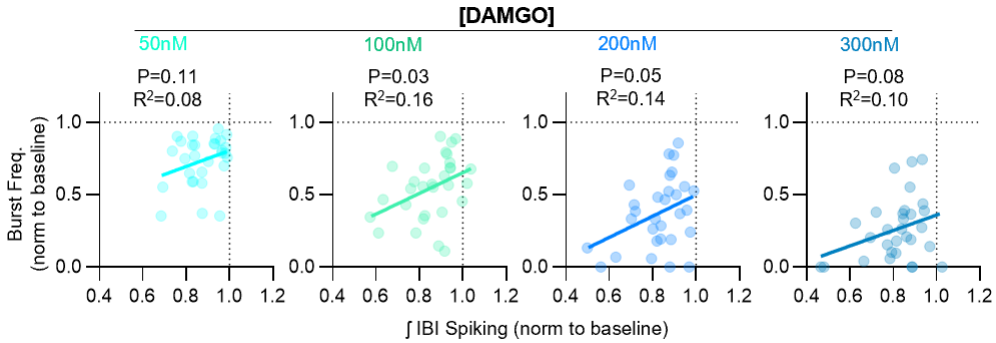

Supplemental Figure 3: Relationships between DAMGO-induced changes in inspiratory burst frequency and integrated inter-burst interval spiking in horizontal brainstem slice preparations. Linear regression analysis.

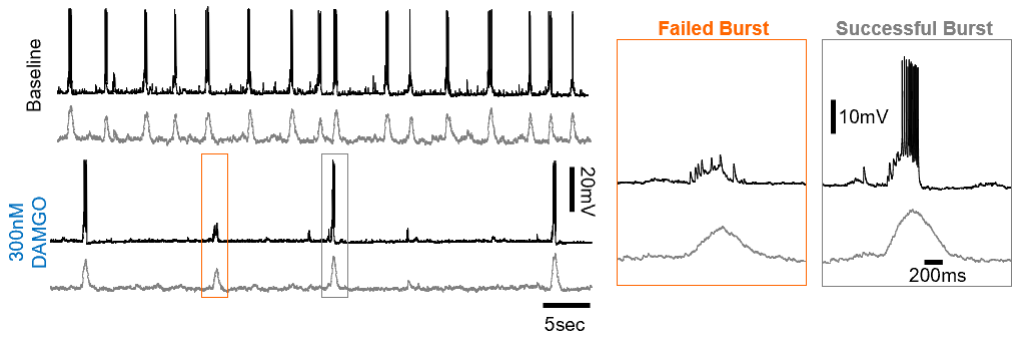

Supplemental Figure 4: Example whole cell recording from an inspiratory neuron (top) and corresponding rhythmic multi-unit activity from the contralateral preBötC at baseline and in 300 nM DAMGO. Note that during failed population bursts in 300 nM DAMGO, the inspiratory neuron receives synaptic inputs that are not sufficient to recruit the neuron to spike.

bioRxiv preprint doi: https://doi.org/10.1101/2021.02.24.432816; this version posted February 25, 2021. The copyright holder for this preprint (which was not certified by peer review) is the author/funder, who has granted bioRxiv a license to display the preprint in perpetuity. It is made available under aCC-BY 4.0 International license.

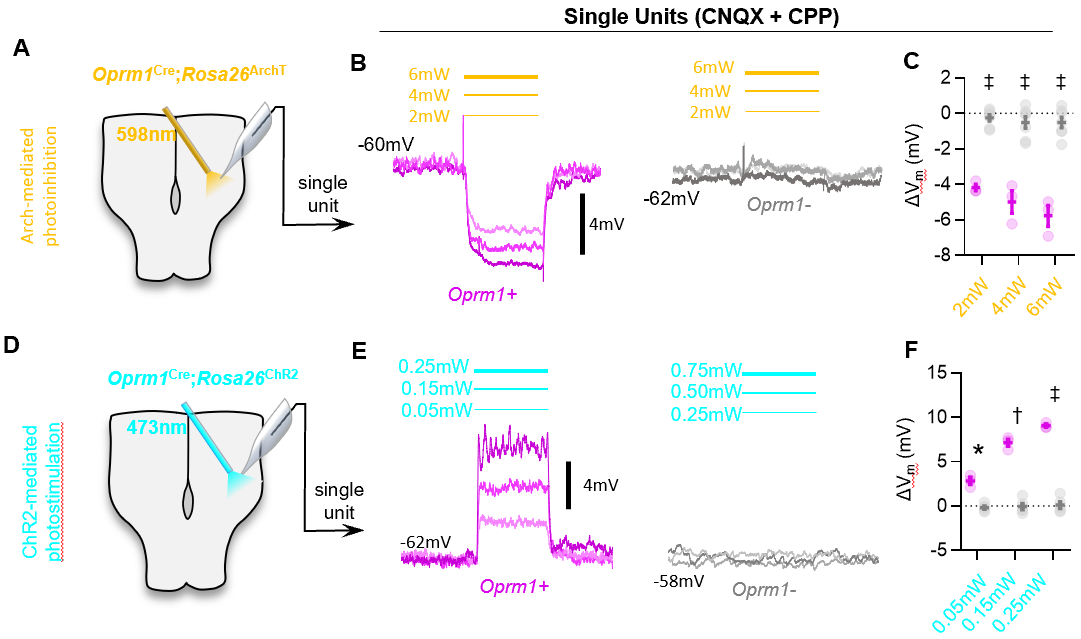

1194 **Supplemental Figure 5:** Optogenetic hyperpolarization and depolarization of *Oprm1*+ preBötC neurons.
1195 **A)** Schematic of experiments in *Oprm1*^{Cre}; *Rosa26*^{ArchT} horizontal brainstem slices. **B)** Example average
1196 membrane potential of an *Oprm1*+ and an *Oprm1*- preBötC neuron during 2mW, 4mW, and 6mW 598nm
1197 light pulses (3-5 trials/power). **C)** Quantified change in membrane potential (ΔV_m) from *Oprm1*+ (n=3) and
1198 *Oprm1*- (n=7) neurons during photoinhibition (two-way RM ANOVA ($p<0.0001$) with Bonferroni's multiple
1199 comparisons tests). **D)** Schematic of *Oprm1*^{Cre}; *Rosa26*^{ChR2} experiments. **E)** Averaged membrane potential
1200 of example *Oprm1*+ and *Oprm1*- preBötC neurons during 0.05, 0.15, and 0.25-mW 473-nm light pulses (3-
1201 5 trials/power). **F)** Quantified ΔV_m from *Oprm1*+ (n=3) and *Oprm1*- (n=5) neurons during photostimulation
1202 (two-way RM ANOVA ($p<0.0001$) with Bonferroni's multiple comparisons tests). Data shown as mean±SE.

1203

1204

1205

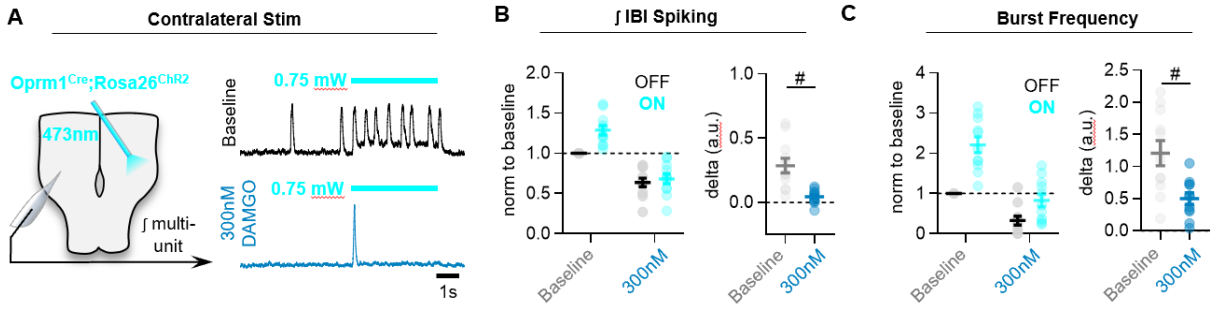

1206 **Supplemental Figure 6:** MOR activation limits the ability of commissural *Oprm1*+ neurons to drive
1207 activity in the contralateral preBötC. **A)** Experimental schematic and representative preBötC recordings at
1208 baseline and in 300 nM DAMGO during a 10-s photostimulaiton of contralateral *Oprm1*+ neurons. **B)**
1209 Quantified effects on inter-burst interval spiking, and **C)** inspiratory burst frequency (two-tailed paired t-
1210 tests). Data shown as mean±SE.

bioRxiv preprint doi: https://doi.org/10.1101/2021.02.24.432816; this version posted February 25, 2021. The copyright holder for this preprint (which was not certified by peer review) is the author/funder, who has granted bioRxiv a license to display the preprint in perpetuity. It is made available under aCC-BY 4.0 International license.

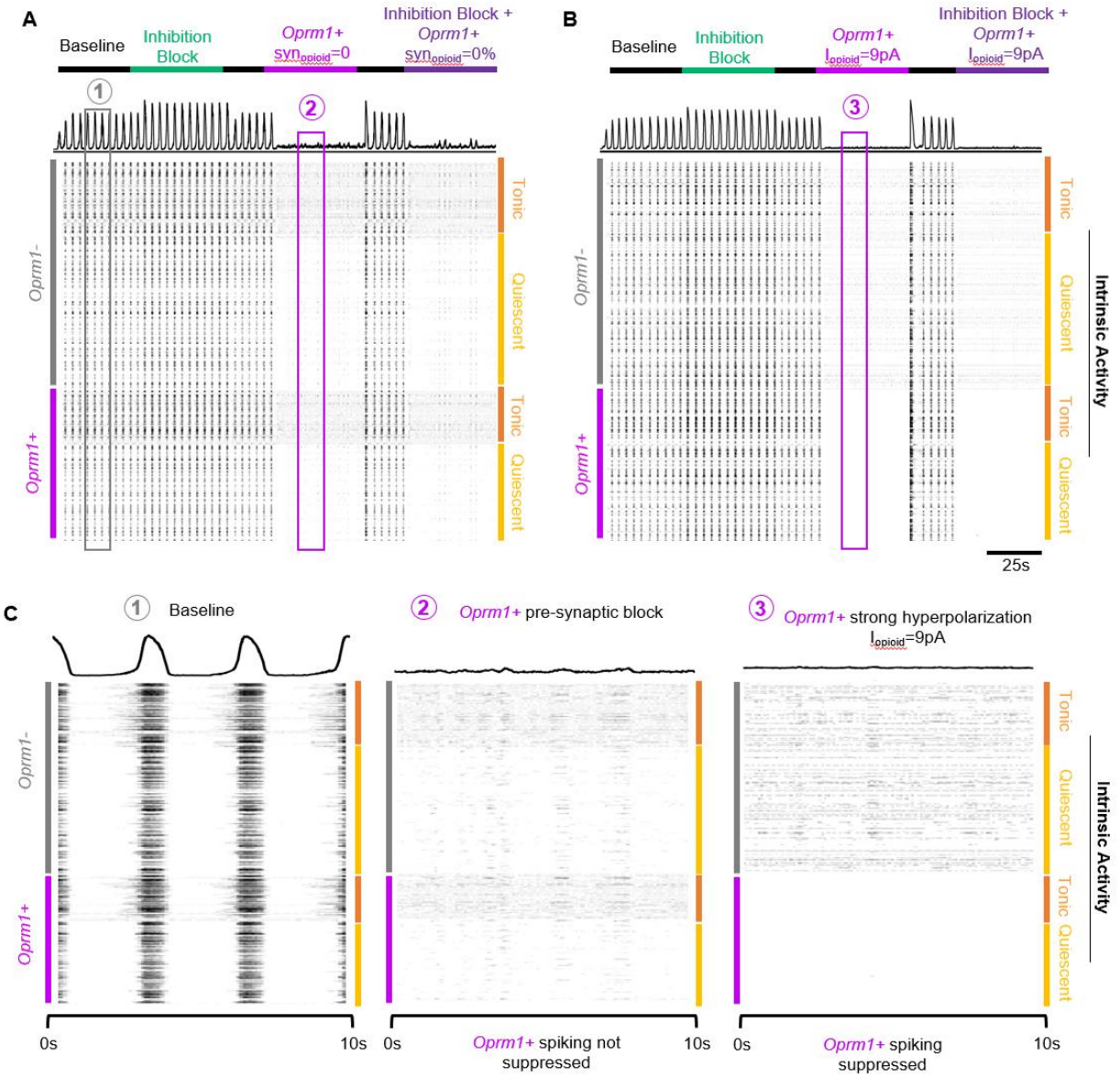

Supplemental Figure 7: A simulated data-driven *Oprm1*+ subpopulation is necessary for rhythmogenesis in an *in silico* preBötC model network. **A)** Example integrated population activity and spike rasters at baseline and during blockade of pre-synaptic transmission from *Oprm1*+ neurons (syn_{opioid}=0) with and without inhibitory synaptic interactions (inhibition block). **B)** Example integrated population activity and spike rasters at baseline and during a strong hyperpolarization (I_{opioid}=9pA) of *Oprm1*+ neurons with and without concurrent blockade of inhibitory synapses. **C)** Expanded view of integrated rhythmic activity and corresponding spike rasters of all 300 model neurons during baseline (left), *Oprm1*+ pre-synaptic block (middle), and strong *Oprm1*+ hyperpolarization (right). Note that in both cases the network rhythm is silenced despite distinct effects on the spiking activity of *Oprm1*+ neurons.

bioRxiv preprint doi: https://doi.org/10.1101/2021.02.24.432816; this version posted February 25, 2021. The copyright holder for this preprint (which was not certified by peer review) is the author/funder, who has granted bioRxiv a license to display the preprint in perpetuity. It is made available under aCC-BY 4.0 International license.

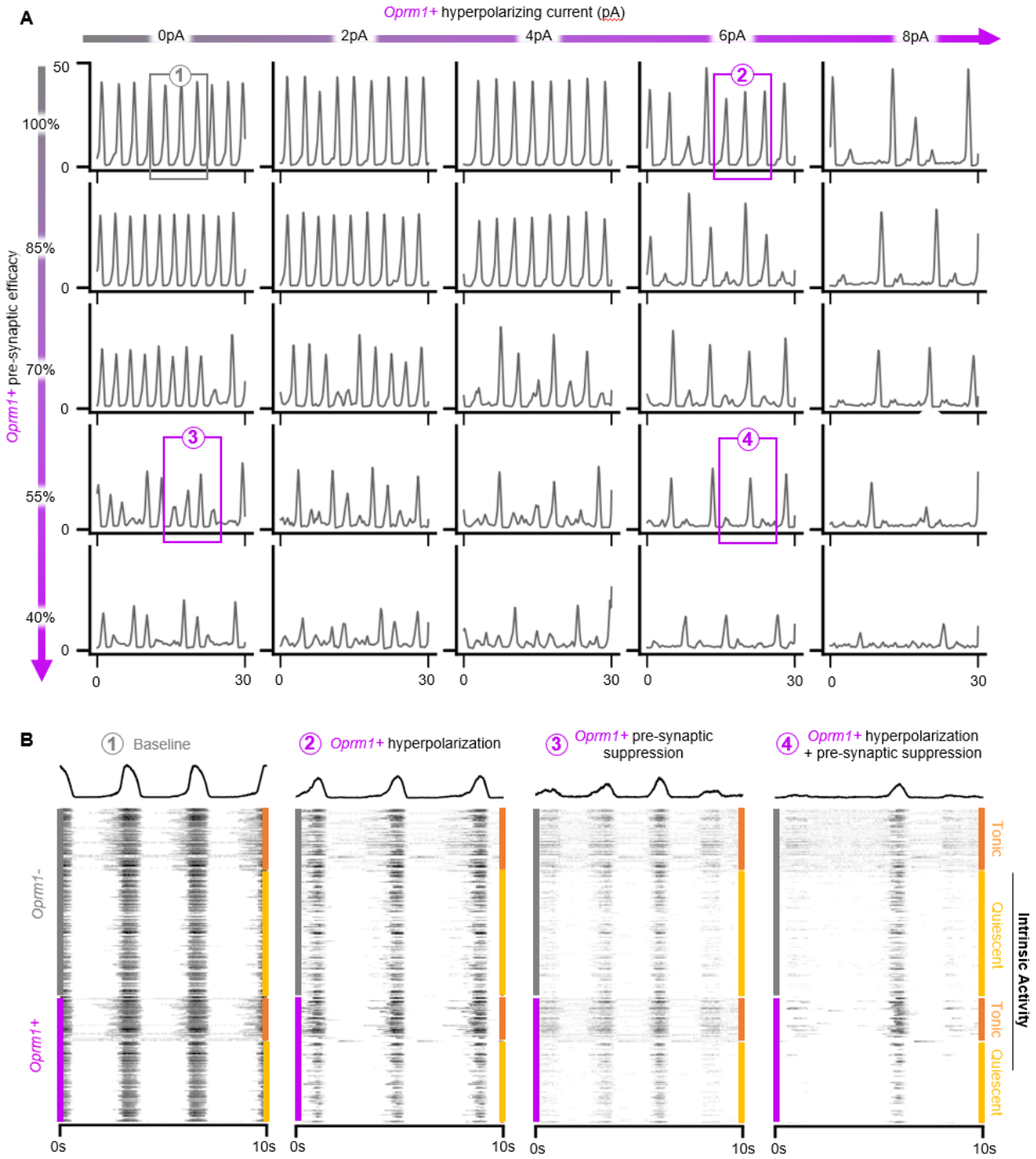

Supplemental Figure 8: OIRD in the preBötC is best modelled by concurrent hyperpolarization and pre-synaptic suppression of a simulated *Oprm1*+ subpopulation. **A)** Rhythmic activity of a representative model network during independent or concurrent *Oprm1*+ neuron hyperpolarization and/or pre-synaptic suppression. **B)** Expanded view of network activities shown in (A) and corresponding spiking activity from all 300 model neurons.

bioRxiv preprint doi: https://doi.org/10.1101/2021.02.24.432816; this version posted February 25, 2021. The copyright holder for this preprint (which was not certified by peer review) is the author/funder, who has granted bioRxiv a license to display the preprint in perpetuity. It is made available under aCC-BY 4.0 International license.

Conductances	
C_m	$21pF$
g_{Na}	$28nS$
g_K	$11.2nS$
g_{NaP}	$\mathcal{N}(0.8, 0.05)nS$
g_E	$4.5nS$
g_I	$4.5nS$

Reversal potentials	
E_{Na}	$50mV$
E_K	$-85mV$
E_{leak}	$-58mV$
E_{synE}	$0mV$
E_{synI}	$-70mV$

Gating and kinetics	
τ_n	$10ms$
τ_h	$10s$
v_m	$-34mV$
v_n	$-29mV$
v_{m_p}	$-40mV$
v_h	$-48mV$
σ_m	$-5mV$
σ_n	$-4mV$
σ_{m_p}	$-6mV$
σ_h	$5mV$
τ_{syn}	$15ms$
θ_s	$0mV$
σ_{syn}	$-3mV$

Supplemental Table 1: Global cell parameters for *in silico* preBötC neurons

N = 300, k_{avg} = 6

20% Inh, 40% $Oprm1^+$, 40% $Oprm1^-$

Neuron Type	g_{leak}	% of Pop.
Tonic	$\mathcal{N}(0.5, 0.05)\ nS$	35%
Quiescent	$\mathcal{N}(1.2, 0.05)\ nS$	65%

Supplemental Table 2: Network parameters for *in silico* preBötC network